

# **Flaw Growth and Flaw Tolerance Assessment for Dry Cask Storage Canisters**

**3002002785**

---



August, 2017

TO: Recipients of EPRI Technical Update 3002002785

Subject: Corrections for 3002002785 *Flaw Growth and Flaw Tolerance Assessment for Dry Cask Storage Canisters*

Our records indicate that you received the subject EPRI product by order or download prior to June 16, 2017. Identification of errors in this product led to initiation of a complete quality review. In addition to the errors, clarifications and quality elements such as use of international units were identified for correction.

The following corrections have been implemented:

- **Section 2.1.3, Footnote 1:** Corrected to indicate that a hypothetical puddle affects the airflow through the overpack (rather than the canister surface), added international units for drying rate.
- **Section 2.2.2:** Added clarification to the bullet describing the assumption used for average internal gas temperature for leakage and ingress calculations.
- **Section 3.2.2, Equation 3-1:** Added international units to definition of  $T_{ref}$ .
- **Section 3.3.2:** Added international units for canister wall thickness.
- **Section 3.3.3:** Added international units for parameters describing operating experience.
- **Section 4.2, 2<sup>nd</sup> Paragraph:** Added clarifications to more accurately describe modeling approach.
- **Section 4.2.1, 2<sup>nd</sup> Paragraph:** Corrected reference citation.
- **Section 4.2.2, 1<sup>st</sup> Paragraph:** Provided additional explanation of assumptions.
- **Section 4.2.3, Multiple Paragraphs:** Revised to provide clarity in description of model assumptions.
- **Tables 4-6, 4-7, and 4-8:** Corrected the “shell thickness” column. Previously, the column label for shell thickness stated millimeters, but the values shown were in inches.
- **Table 4-7 and 4-8:** Corrected the results columns for the ingress case results tables. An error was identified in the calculation; properties for pure helium were being applied to the air/gas mixture flowing out of the canister, affecting the calculated molar flow rate, this was corrected and the results were updated.
- **Figure 4-3:** Figure updated to reflect corrected ingress calculations.
- **Section A.4.1:** the citation at the end of the first paragraph should refer to Reference 10 (*SQUIRT: Seepage Quantification of Upsets In Reactor Tubes User's Manual*) instead of Reference 49.

Together . . . Shaping the Future of Electricity

**PALO ALTO OFFICE**

3420 Hillview Avenue, Palo Alto, CA 94304-1338 USA • 650.855.2000 • Customer Service 800.313.3774 • [www.epri.com](http://www.epri.com)

The following errors in the original issue of this technical update were previously corrected in a notice on April 15, 2016:

- **Table 3-4:** corrected the *Surface Temp. at Crack Initiation* column, the Ambient temperature, and the *Time to Grow* data for Case 10.
- **Figure 3-11:** corrected the caption to read, “Decay Power Curve for Cases in Table 3-3 and Table 3-4 (Generated for 10 Assemblies of 40 GWd/MTHM After Wet Storage for 10 yr and 14 Assemblies of 30 GWd/MTHM After Wet Storage for 15 yr).”
- **Table 4-5:** Corrected value in *Multiples of Shell Thickness* column for Case 2, value in *Design Internal Pressure* column for Case 4, and value in *Crack Opening Area – Axial* for Case 2.
- **Equation 4-3:** replaced equation to eliminate errors in printing.
- **Equation A-5:** updated equation for accuracy.
- **Section A.2.2.2:** corrected spelling of “Arrhenius.”

# Flaw Growth and Flaw Tolerance Assessment for Dry Cask Storage Canisters

3002002785

Technical Update, October 2014

EPRI Project Manager

S. Chu

All or a portion of the requirements of the EPRI Nuclear Quality Assurance Program apply to this product.

YES



## **DISCLAIMER OF WARRANTIES AND LIMITATION OF LIABILITIES**

THIS DOCUMENT WAS PREPARED BY THE ORGANIZATION(S) NAMED BELOW AS AN ACCOUNT OF WORK SPONSORED OR COSPONSORED BY THE ELECTRIC POWER RESEARCH INSTITUTE, INC. (EPRI). NEITHER EPRI, ANY MEMBER OF EPRI, ANY COSPONSOR, THE ORGANIZATION(S) BELOW, NOR ANY PERSON ACTING ON BEHALF OF ANY OF THEM:

(A) MAKES ANY WARRANTY OR REPRESENTATION WHATSOEVER, EXPRESS OR IMPLIED, (I) WITH RESPECT TO THE USE OF ANY INFORMATION, APPARATUS, METHOD, PROCESS, OR SIMILAR ITEM DISCLOSED IN THIS DOCUMENT, INCLUDING MERCHANTABILITY AND FITNESS FOR A PARTICULAR PURPOSE, OR (II) THAT SUCH USE DOES NOT INFRINGE ON OR INTERFERE WITH PRIVATELY OWNED RIGHTS, INCLUDING ANY PARTY'S INTELLECTUAL PROPERTY, OR (III) THAT THIS DOCUMENT IS SUITABLE TO ANY PARTICULAR USER'S CIRCUMSTANCE; OR

(B) ASSUMES RESPONSIBILITY FOR ANY DAMAGES OR OTHER LIABILITY WHATSOEVER (INCLUDING ANY CONSEQUENTIAL DAMAGES, EVEN IF EPRI OR ANY EPRI REPRESENTATIVE HAS BEEN ADVISED OF THE POSSIBILITY OF SUCH DAMAGES) RESULTING FROM YOUR SELECTION OR USE OF THIS DOCUMENT OR ANY INFORMATION, APPARATUS, METHOD, PROCESS, OR SIMILAR ITEM DISCLOSED IN THIS DOCUMENT.

REFERENCE HEREIN TO ANY SPECIFIC COMMERCIAL PRODUCT, PROCESS, OR SERVICE BY ITS TRADE NAME, TRADEMARK, MANUFACTURER, OR OTHERWISE, DOES NOT NECESSARILY CONSTITUTE OR IMPLY ITS ENDORSEMENT, RECOMMENDATION, OR FAVORING BY EPRI.

THE FOLLOWING ORGANIZATION, UNDER CONTRACT TO EPRI, PREPARED THIS REPORT:

**Dominion Engineering Inc.**

THE TECHNICAL CONTENTS OF THIS PRODUCT WERE **NOT** PREPARED IN ACCORDANCE WITH THE EPRI QUALITY PROGRAM MANUAL THAT FULFILLS THE REQUIREMENTS OF 10 CFR 50, APPENDIX B. THIS PRODUCT IS **NOT** SUBJECT TO THE REQUIREMENTS OF 10 CFR PART 21.

**This is an EPRI Technical Update report. A Technical Update report is intended as an informal report of continuing research, a meeting, or a topical study. It is not a final EPRI technical report.**

### **NOTE**

For further information about EPRI, call the EPRI Customer Assistance Center at 800.313.3774 or e-mail [askepri@epri.com](mailto:askepri@epri.com).

Electric Power Research Institute, EPRI, and TOGETHER...SHAPING THE FUTURE OF ELECTRICITY are registered service marks of the Electric Power Research Institute, Inc.

Copyright © 2014 Electric Power Research Institute, Inc. All rights reserved.

# ACKNOWLEDGMENTS

The following organization, under contract to the Electric Power Research Institute (EPRI), prepared this report:

Dominion Engineering Inc.  
12100 Sunrise Valley Drive, Suite 220  
Reston, Virginia 20191

Principal Investigators

K. Fuhr

J. Broussard

G. White

This report describes research sponsored by EPRI.

---

This publication is a corporate document that should be cited in the literature in the following manner:

*Flaw Growth and Flaw Tolerance Assessment for Dry Cask Storage Canisters*. EPRI, Palo Alto, CA: 2014. 3002002785.



# PRODUCT DESCRIPTION

The majority of dry cask storage systems (DCSSs) in the United States confine used nuclear fuel within austenitic stainless steel canisters, and there is concern that some of these may become susceptible to chloride-induced stress corrosion cracking (CISCC) over the extended timeframe of their storage at independent spent fuel storage installations (ISFSIs). This report is part of an industry effort to evaluate the susceptibility to CISCC of stainless steel canisters used in DCSSs.

## Background

Due to the delayed opening of a final geological repository for used fuel generated by U.S. nuclear power plants, many plants have constructed an ISFSI, using DCSSs to relieve crowding in the spent fuel pool. To address concerns that corrosion of the stainless steel canisters may occur at some sites over extended periods of operation (on the order of 120 years or longer), the Electric Power Research Institute (EPRI) is developing an aging management plan with susceptibility criteria for stainless steel canisters.

## Objective

The objective of this technical update is to calculate the time frames associated with the progression of CISCC in austenitic stainless steel canisters in DCSSs, starting with the assumption that it has initiated. This report also evaluates the tolerance of the canister to a through-wall crack. Modeling and calculations are performed that: (1) determine the growth rate of CISCC cracking (starting after the assumed point of crack initiation), (2) evaluate the effect of different ambient environments on crack growth rates, (3) calculate the mechanical flaw tolerance of the canister, and (4) determine the time taken for air to displace the inert internal atmosphere of the canister.

## Approach

The flaw growth assessment first describes a crack growth rate model based on the available experimental data for atmospheric CISCC. Environmental data are then used to calculate the propagation rates, assuming prior crack initiation, that result from the duration of aqueous conditions and surface temperature calculated for various climates. This model is applied to calculate the time to propagate through the shell thickness for various locations on a hypothetical canister, starting immediately after CISCC initiation. In the flaw tolerance assessment, critical crack sizes are calculated for design basis pressure and handling loads, and representative time scales for air ingress are calculated.

## Results

Due to the relationship between surface temperature, humidity, and deliquescence, crack growth rates are dependent on the local atmospheric conditions, and calculated through-wall crack propagation times vary greatly among locations with different ambient conditions. The time required to develop conditions conducive to SCC and potentially lead to crack initiation is not evaluated in this report.

CISCC initiation is dependent on site-specific environmental conditions and the decay heat loading of each canister, and initiation would likely require a substantial period of time. The canister designs are very flaw tolerant; large flaws are required before a critical flaw size is approached. Once a flaw grows through-wall, the depressurization time is calculated to be

relatively short, while the time required for air to displace the inert backfilled atmosphere is months or years.

### **Application, Value, and Use**

These analyses are presented in advance of the Industry Susceptibility Assessment Criteria report, which will consider how the canister's flaw tolerance affects schedules for evaluation and how environmental and DCSS parameters affect the full cycle of CISCC degradation, that is, establishment of susceptible conditions, followed by CISCC propagation,. The model and calculation framework developed in this evaluation may be further extended to perform risk-based evaluations of aging management strategies.

### **Keywords**

Chloride-induced stress corrosion cracking (CISCC)

Dry cask storage system (DCSS)

Failure modes and effects analysis (FMEA)

Multi-purpose canister

Stainless steel welded canister

Used nuclear fuel storage

## **ABSTRACT**

This technical update documents the modeling and calculations performed to evaluate the propagation of chloride-induced stress corrosion cracking in austenitic stainless steel canisters in dry cask storage systems and the mechanical tolerance of the system for this degradation. A crack growth rate model was developed using data from published literature, and the model was used to calculate the time required for a crack to grow through-wall. The ability of the canister to tolerate a through-wall flaw was assessed against structural limit criteria using typical canister loads. Additionally, hypothesizing a through-wall flaw, the timescale required for replacement of the inert backfill with ambient air was investigated.



# ACRONYMS

AFB	Air Force Base
AH	Absolute Humidity
ASME	American Society of Mechanical Engineers
BWR	Boiling Water Reactor
CFD	Computational Fluid Dynamics
CGR	Crack Growth Rate
CISCC	Chloride-Induced Stress Corrosion Cracking
COA	Crack Opening Area
COD	Crack Opening Displacement
CRIEPI	Central Research Institute of Electric Power Industry
CT	Compact Tension
DCPD	Direct Current Potential Drop
DCSS	Dry Cask Storage System
DRH	Deliquescence Relative Humidity
ECCS	Emergency Core Cooling System
EPRI	Electric Power Research Institute
ERH	Efflorescent Relative Humidity
FMEA	Failure Modes and Effects Analysis
HAZ	Heat Affected Zones
HI-STORM	Holtec International Storage and Transfer Operation Reinforced Module
IGSCC	Intergranular Stress Corrosion Cracking
ISFSI	Independent Spent Fuel Storage Installation
MAGNASTOR	Modular Advanced Generation Nuclear All-purpose STORAGE
MRP	Materials Reliability Program
MTHM	Metric Ton of Heavy Metal
NAC	NAC International
NASA	National Aeronautics and Space Administration

NOAA	National Oceanic and Atmospheric Administration
NPS	Nominal Pipe Size
NRC	U.S. Nuclear Regulatory Commission
NUHOMS	Nutech Horizontal Modular Storage
OD	Outer Diameter
ODSCC	Outer Diameter Stress Corrosion Cracking
ORIGEN	Oak Ridge Isotope Generation and Depletion
PD	Part-Depth
PNNL	Pacific Northwest National Laboratory
PWR	Pressurized Water Reactor
RAI	Request for Additional Information
RH	Relative Humidity
RWST	Refueling Water Storage Tank
SAR	Safety Analysis Report
SCC	Stress Corrosion Cracking
SCH	NPS Piping Schedule
SQUIRT	Seepage Quantification of Upsets In Reactor Tubes
TW	Through-Wall
UMS	Universal Modular Storage
WRS	Weld Residual Stress

# CONTENTS

<b>1 INTRODUCTION .....</b>	<b>1-1</b>
1.1 Background .....	1-1
1.2 Objective .....	1-1
1.3 Scope .....	1-1
1.4 Approach .....	1-2
1.5 Report Structure .....	1-2
<b>2 KEY MODELING INPUTS AND ASSUMPTIONS .....</b>	<b>2-1</b>
2.1 Flaw Growth Assessment .....	2-1
2.1.1 Flaw Location and Orientation .....	2-1
2.1.2 Crack Growth Rate (CGR) Equation .....	2-2
2.1.3 Ambient Temperature and Humidity .....	2-3
2.2 Flaw Tolerance Assessment .....	2-4
2.2.1 Critical Crack Size .....	2-4
2.2.2 Gas Leakage .....	2-5
2.3 Thermal Analysis Data .....	2-6
<b>3 CRACK GROWTH MODELING .....</b>	<b>3-1</b>
3.1 Expected Flaw Growth Characteristics .....	3-1
3.2 Chloride-Induced SCC Flaw Growth Model .....	3-4
3.2.1 CGR Coefficient for Atmospheric CISCC .....	3-4
3.2.2 CISCC CGR Equation .....	3-7
3.3 Model Results .....	3-10
3.3.1 Crack Growth Rates for Various Climates .....	3-10
3.3.2 Flaw Growth Results .....	3-12
3.3.3 Comparison with Relevant Operating Experience .....	3-16
<b>4 FLAW TOLERANCE ASSESSMENT .....</b>	<b>4-1</b>
4.1 Flaw Size Tolerance .....	4-1
4.1.1 Load Cases .....	4-1
4.1.2 Critical Flaw Size and Net Section Collapse .....	4-2
4.2 Tolerance for Loss of Helium Backfill .....	4-5
4.2.1 Crack Opening Area .....	4-5
4.2.2 Helium Leakage .....	4-8
4.2.3 Air Ingress .....	4-10
<b>5 CONCLUSIONS .....</b>	<b>5-1</b>
5.1 Flaw Propagation Calculation .....	5-1
5.2 Flaw Tolerance Evaluation .....	5-1
5.3 Modeling Considerations .....	5-2
<b>6 REFERENCES .....</b>	<b>6-1</b>
<b>A MODEL DETAILS AND INPUTS .....</b>	<b>A-1</b>

A.1 Humidity, Climate, and Deliquescence ..... A-1  
    A.1.1 Deliquescence Model ..... A-1  
    A.1.2 Process to Obtain Hourly Local Climate Data..... A-3  
A.2 Crack Growth Rate ..... A-4  
    A.2.1 CGR Equation Structure ..... A-4  
    A.2.2 CGR Equation Parameters ..... A-6  
    A.2.3 Statistical Treatment of Growth Rate Parameters ..... A-12  
A.3 Thermal Analysis Data..... A-16  
    A.3.1 Fuel Assembly Decay Power ..... A-16  
    A.3.2 Canister Temperatures ..... A-17  
A.4 Gas Transmission Between Canister and Environment ..... A-18  
    A.4.1 Leak Rate ..... A-18  
    A.4.2 Ingress due to Temperature and Pressure Fluctuations..... A-19

# LIST OF FIGURES

Figure 2-1 Aspects of Flaw Initiation and Growth (Relative Time Durations Not to Scale) .....	2-1
Figure 3-1 Diagram of Idealized Part-Depth Flaw Growth (Tensile Stress is Normal to the Page).....	3-3
Figure 3-2 Representative Canister Weld Configuration .....	3-3
Figure 3-3 DCPD Data Showing Two-Phase Growth (Reprinted from [30]) .....	3-3
Figure 3-4 Cumulative Distribution for CISCC Experiments Reporting CGR Data for Sea Salt ([20] and [6]), in Shallow Cracks (First Phase Growth) .....	3-6
Figure 3-5 Cumulative Distribution for CISCC Experiments Reporting CGR Data for Sea Salt [6], in Deep Cracks (Second Phase Growth) .....	3-6
Figure 3-6 Canister Surface Temperature Calculated from the Atmospheric Temperature, Plotted with the Absolute Humidity, First Week of August 2011, Camp Pendleton, CA .....	3-9
Figure 3-7 Plot of Surface RH and DRH for Conditions in Figure 3-6 and the Resultant CGR..	3-9
Figure 3-8 Average of the Environmental Factor on CGR ( $f_{RH}$ ) Based on One Year of Hourly Climate Data for Different Locations .....	3-11
Figure 3-9 Crack Depth vs. Time for South East (Homestead AFB, FL) Cases in Table 3-3 ..	3-15
Figure 3-10 Crack Depth vs. Time for West Coast (Camp Pendleton, CA) Cases in Table 3-3 .....	3-15
Figure 3-11 Decay Power Curve for Cases in Table 3-3 and Table 3-4 (Generated for 10 Assemblies of 40 GWd/MTHM After Wet Storage for 10 yr and 14 Assemblies of 30 GWd/MTHM After Wet Storage for 15 yr) .....	3-16
Figure 4-1 Diagram of Crack Opening for Idealized Through-Wall Flaw .....	4-8
Figure 4-2 Results of Leakage Analysis for Case 7 of Table 4-6.....	4-10
Figure 4-3 Results of Air Ingress Analysis for Case 1 of Table 4-8 .....	4-13
Figure A-1 DRH Model, CNWRA Sea Salt DRH Data [8], and Standard DRH Curves for Various Salts [45] Plotted for Temperature and RH on Curves of Constant AH .....	A-2
Figure A-2 Fraction of Year that the Humidity at Different Monitoring Sites [7] is at or above a Given Value of AH.....	A-4
Figure A-3 Arrhenius Plot for Crack Depth Growth Rate at RH = (Left) 35% and (Right) 55% for the Mean and Maximum Values (Remade from the Data of Reference [52] © NACE International 2008) .....	A-7
Figure A-4 Duty Cycle by Baseline Canister Surface Temperature for Coastal Monitoring Stations .....	A-9
Figure A-5 $K_I$ vs. Depth for a Flaw in a Plate 10 mm Thick, Subject to 270 MPa Bending .....	A-12
Figure A-6 Cumulative Log-Normal Distribution for CISCC Experiments Reporting CGR Data for Sea Salt ([20] and [6]), in Shallow Cracks (First Phase Growth) .....	A-15
Figure A-7 Cumulative Log-Normal Distribution for CISCC Experiments Reporting CGR Data for Sea Salt [6], in Deep Cracks (Second Phase Growth) .....	A-15
Figure A-8 Cumulative Normal Distribution for the Transition Depth Seen in CISCC Experiments Reporting CGR Data for Sea Salt [6] .....	A-16
Figure A-9 Decay Power per Assembly Curves for Different Burnups of PWR and BWR Fuel .....	A-17



# LIST OF TABLES

Table 3-1 Statistics for the Upper Bound of the 50% Confidence Interval Log-Normal Fit to the Data at 80°C in Figure 3-4 and Figure 3-5.....	3-5
Table 3-2 Locations and Key Information for Climate Data from Reference [7] Analyzed in this Technical Update.....	3-11
Table 3-3 Crack Growth Analysis Results for Varying Climates and Initial Surface Temperature Offsets.....	3-13
Table 3-4 Crack Growth Analysis Sensitivity Cases.....	3-14
Table 4-1 Load Cases Considered in this Section (Note 2).....	4-2
Table 4-2 Results for Part Depth (PD) and Through-Wall (TW) Critical Flaw Size Calculations.....	4-4
Table 4-3 Critical Flaw Size for Normal Handling Loads Only (No Internal Pressure).....	4-5
Table 4-4 Weld Residual Stress Values [1] Used in the Crack Opening Displacement Analysis.....	4-7
Table 4-5 Crack Opening Area Results for Larger of Seam and Girth Weld Cases for Bounding Canister Designs.....	4-7
Table 4-6 Leak Rate Inputs and Results.....	4-9
Table 4-7 Ingress Cases for Large Sinusoidal Daily Temperature Variation.....	4-12
Table 4-8 Ingress Cases Using Measured Hourly Atmospheric Pressure and Temperature Data.....	4-12



# 1

## INTRODUCTION

### 1.1 Background

Aqueous chlorides are capable of creating localized breaches in the surface oxide layer of stainless steels, leading to localized corrosion. In the presence of sufficient stress, chloride-induced stress corrosion cracking (CISCC) can develop and propagate through the material. Limited instances of cracking of austenitic stainless steel piping at ocean shore nuclear power plants indicates that contamination by atmospheric chlorides can be sufficient to lead to CISCC. The majority of dry cask storage systems (DCSSs) in the U.S. confine the spent nuclear fuel within austenitic stainless steel canisters, and there is concern that some of these may become susceptible to CISCC over the extended timeframe of their storage at independent spent fuel storage installations (ISFSIs).

This assessment is part of an industry effort to evaluate the susceptibility to CISCC of stainless steel canisters used in DCSSs. A failure modes and effects analysis (FMEA) [1] evaluated the atmospheric corrosion processes and other degradation mechanisms that may be active on canister surfaces and identified CISCC as the most credible atmospheric corrosion mechanism for through-wall penetration, based on current knowledge. A literature review [2] was produced which focused on characterizing the establishment of susceptible conditions, time to initiation, and propagation rate of chloride-induced degradation mechanisms for stainless steel.

### 1.2 Objective

The objectives of this technical update are:

- Using currently available data, develop a quantitative model for the growth rate of CISCC flaws following a postulated initiation
- Evaluate the effect of different ambient environments on the predicted flaw propagation rates
- Determine the structural tolerance of the canister to flaws of varying size
- Calculate approximate helium leak rates and air ingress rates for different flaw sizes

### 1.3 Scope

The scope of this investigation considers through-wall degradation due to CISCC of the stainless steel canisters used as the confinement boundary for many DCSSs. The findings of References [1] and [2] indicate that CISCC is the most credible corrosion mechanism that could cause penetration of the canister within the first 120 years of storage. In this evaluation, it is postulated that flaw initiation has already occurred, and modeling the progression of degradation is limited to flaw propagation. To add context to the flaw growth analysis, critical flaw sizes and the timeframe for replacement of the canister's inert backfill gas with air are calculated.

## 1.4 Approach

The flaw growth assessment first describes a crack growth rate model based on the available experimental data for atmospheric CISCC. Environmental data is then used to calculate the propagation rates, assuming prior crack initiation, resulting from the duration of aqueous conditions and surface temperature calculated for various climates. This model is applied to calculate time to propagate through the shell thickness for various locations on a hypothetical canister, starting immediately after CISCC initiation. In the flaw tolerance assessment, critical crack sizes are calculated for design basis pressure and handling loads, and representative timescales for air ingress are calculated.

## 1.5 Report Structure

This technical basis report is organized as follows:

1. Introduction (Section 1)  
Introduces the potential for corrosion of DCSS canisters due to atmospheric chlorides, and presents the objective, approach, and organization of this technical update to evaluate that possibility.
2. Key-Modeling Inputs and Assumptions (Section 2)  
Identifies and discusses the basis for key assumptions in the development of the assessment, and also identifies key inputs.
3. Crack Growth Modeling (Section 3)  
Describes modeling of the propagation of CISCC flaws through the stainless steel shell of the DCSS canister.
4. Flaw Tolerance Assessment (Section 4)  
Considers the critical crack sizes for different stored canisters as well as the leak rate and timescale for air ingress for various size flaws in the canister.
5. Conclusions (Section 5)  
Provides a summary of the analyses and key results.
6. References (Section 6)  
Contains the list of references cited in the technical update
- A. Model Details and Inputs (Appendix A)  
Contains a detailed description of the models and equations used in the analyses in the main body of the report.

# 2

## KEY MODELING INPUTS AND ASSUMPTIONS

This section describes the key inputs and assumptions which influence the approach used to assess the flaw growth and flaw tolerance of DCSS canisters. Each of the flaw growth and the flaw tolerance sections are divided according to the calculations performed as a part of those assessments. A short description of the basis for each input and assumption is provided in this section, and a more complete substantiation is provided in the context of the analyses in Sections 3 and 4.

### 2.1 Flaw Growth Assessment

The flaw growth assessment provides a deterministic assessment of the crack growth phase of degradation of stainless steel by CISC. The time frame covered by this assessment is shown in the indicated portion of Figure 2-1. While the time required for each the three phases shown will vary depending on a number of factors, the crack growth phase would occur only after the point of crack initiation; i.e., a flaw of engineering significance is present. The storage duration at which cracking may initiate is expected to be substantial and will depend on factors such as chloride aerosol concentrations and surface orientation.

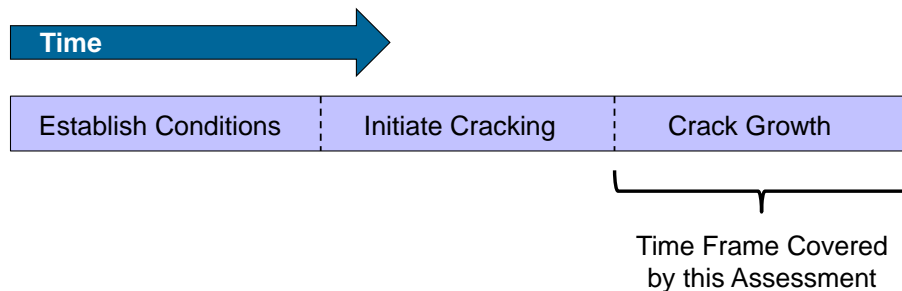


**Figure 2-1**  
**Aspects of Flaw Initiation and Growth (Relative Time Durations Not to Scale)**

#### 2.1.1 Flaw Location and Orientation

The following assumptions apply to the initial state of the crack growth calculations:

- SCC growth is expected to occur near welds due to the presence of elevated tensile through-wall residual stress conditions and a more susceptible material condition [1].
- The data used in this crack growth assessment is from experiments with cracks growing in an atmospherically exposed material. Once the crack grows to macroscopic levels, it can be expected that the solution within the crack is chemically isolated relative to the external solution [3] such that crack growth that initiates at a pit, crevice, or surface is roughly equivalent.
- The weld material itself is expected to be less susceptible due to higher levels of  $\delta$ -ferrite [4]. Initiation testing of welded specimens generally confirms that initiation and most propagation occurs outside the weld metal.

- Based on welding residual stress analyses in Appendix A of the FMEA [1], the most likely flaw orientation is perpendicular to the weld axis. Axial and circumferential flaws are both possible since canisters have both circumferential and axial welds. The length of flaws growing transverse to the weld is expected to be limited to the region of tensile stress.

It is noted that much of the canister surfaces are subject to conditions that would inhibit or prohibit crack initiation due to: (1) the lack of deliquescence due to elevated temperatures in the axial center of horizontal canisters and the upper end of vertical canisters, (2) the lack of sufficient tensile stress likely to cause initiation and growth in regions beyond about four shell thicknesses from the weld, or (3) the lack of sufficient chloride deposits to cause CISC propagation.

### **2.1.2 Crack Growth Rate (CGR) Equation**

The development of a crack growth rate equation for atmospheric CISC of austenitic stainless steels is summarized in Section 3.2 and described in detail in Section A.2. The CGR equation consists of a crack growth rate coefficient multiplied by factors that account for the conditions at the crack. In this model, different coefficients are developed for crack growth before and beyond a threshold depth. Each coefficient is developed in a statistically conservative fashion considering both uncertainty in the mean and the distribution of the data.

#### **Inputs**

- The development of the crack growth rate equation is supported by the findings in the recent EPRI literature review on CISC of stainless steels [2].
- CISC requires an aqueous environment to be active; therefore, no growth from CISC can occur when the deposited chlorides are dry (e.g., when the RH around a hygroscopic salt decreases below the efflorescent RH). See further discussion in Section A.1.1 and Section A.2.2.5.
- Based on residual stress analyses in Appendix A of the FMEA [1], through-wall stresses sufficient for crack initiation and growth are present in the vicinity of welds (within about four wall thicknesses on each side of the weld centerline). As described in greater detail in Section 3, there is effectively no dependence of CGR on the crack tip stress intensity factor ( $K_I$ ) in the data sets evaluated [5]. Therefore, the CGR model is currently independent of the magnitude of tensile stress present.

#### **Assumptions**

- The CGR of CISC is related to the material temperature by an Arrhenius relation. This assumption is based on the common dependence of SCC propagation on temperature as found in correlations used in industry, code, and theoretical work.
- The data used to establish the parameter values for the CGR equation are developed from experiments where the specimens are doped with sea salt and for which crack growth rate is calculated without including the time to initiation. Sea salt is expected to behave closest to the deposits on canisters located in marine environments, and is generally conservative for deliquescence and growth relative to pure sodium chloride.
- Crack growth is assumed to follow the two-phase growth behavior observed in Reference [6]. The rapid bi-linear transition in growth is modeled by switching the CGR coefficient once a crack grows deeper than a threshold depth as described in Section A.2.2.5.

- The crack growth model assumes that crack growth only occurs when the RH—based on the canister surface temperature and the absolute humidity—is at and above a temperature-dependent value for the deliquescence point. A conservative lower bound value for this deliquescence point is used as described in Section 2.1.3 below.
- The CGR is assumed to be independent of chloride areal density due to a lack of CGR testing with different chloride areal densities. This is a conservative assumption since the underlying data for the CGR coefficient comes from specimens doped with elevated chloride areal densities (about 10 g/m<sup>2</sup>). It is expected that the CGR would decrease dramatically at lower areal densities resulting in a deliquescent film that is sparse enough to rate limit or disrupt the reaction at the cathodic site on the surface.
- The current data do not justify different CGR coefficients or equations for different alloys of austenitic stainless steel used in canisters (e.g., Type 304 and Type 316). However, time to initiation data does indicate 316 and low-carbon alloys are less susceptible to crack initiation.
- The crack growth rate model is based on low cold work specimens without surface abuse (e.g., abusive grinding), and canister material is assumed to have a comparable material condition.

### **2.1.3 Ambient Temperature and Humidity**

Ambient temperature and humidity are used as inputs to the flaw growth calculations. The ambient temperature sets the canister surface temperature at a given power, and the canister surface temperature is used to calculate the temperature-adjusted crack growth rate. Additionally, the canister temperature combined with the ambient humidity is used to determine the times at which any deposited salts would be deliquescent and therefore cause flaw propagation to occur.

#### **Inputs**

- Hourly climate data (including ambient temperature and dew point) for a wide range of monitoring station locations can be obtained from NOAA at Reference [7].
- The values for the deliquescent relative humidity (DRH) of sea salt is based on recent deliquescence testing [8] and is supported by results from initiation testing of specimens doped with sea salt. Additional discussion on deliquescence is provided in Section A.1 and supported by Figure A-1.

#### **Assumptions**

- The deliquescence point used for sea salt in the crack growth calculations is conservatively established to bound the efflorescent relative humidity (ERH, lower than the DRH), as discussed in Section A.1.1. Therefore, the deliquescence point at all temperatures is chosen to be a conservative, lower bound value. This conservative assumption is applied to account for effects not explicitly modeled in this calculation, such as drying time and hysteresis between deliquescence and efflorescence.
- Extrapolating from available data, the temperature dependence of the DRH of sea salt is assumed to mirror that of MgCl<sub>2</sub> with a 7% offset. The offset maintains a DRH below measured ERH values for sea salt.
- Conservatively benchmarking the humidity threshold for crack propagation relative to the DRH of sea salt and MgCl<sub>2</sub> is conservative considering the other prevalent species in atmospheric aerosols. DRH testing of other salts present in the atmosphere (e.g., ammonium

salts and sulfate salts) demonstrated that their DRH values and the mutual DRH of  $\text{NH}_4\text{NO}_3$  plus NaCl are above that of sea salt and  $\text{MgCl}_2$  [8].

- The absolute humidity (AH) within the overpack is assumed to be identical to the ambient atmospheric value. The airflow through the canister overpack is on the order of  $0.3 \text{ m}^3/\text{s}$ , and this constantly refreshing environment limits the ability of any water that may be inside the overpack to increase the local humidity beyond ambient.<sup>1</sup> Regular walk-down inspection of inlet screens for blockage ensures the buoyancy-driven airstream is not obstructed.
- Local environmental data (RH and temperature) are taken from atmospheric monitoring stations located near representative ISFSI locations. For the scope and scale of the calculations performed, the environmental data at the monitoring location is considered an accurate first order representation of the environment at the nearby ISFSI location.

## 2.2 Flaw Tolerance Assessment

### 2.2.1 Critical Crack Size

The flaw tolerance of the canister from a structural standpoint is evaluated based on critical crack size calculations established in the ASME Code Section XI.

#### Inputs

- Canister geometry and load cases are based on the values reported in DCSS design Safety Analysis Reports (SARs).
- Critical crack size is evaluated using the ASME Boiler and Pressure Vessel Code Section XI Appendix C process for austenitic base material, which uses limit load criteria.

#### Assumptions

- Based on the crack growth information presented in Section 3, flaws are likely to grow in depth at the same rate as each surface edge. Therefore, flaws that reach through-wall are likely to be equal in length to two times the wall thickness. Based on the semi-circular crack in post-test fracture plane imaging [6], it is expected that crack growth on the surface also slows after the depth transition.
- Four idealized crack morphologies are considered in the evaluations of the cylindrical shell. Through-wall cracks of a finite length are considered, in both circumferential and axial orientations. Also considered are arbitrarily long flaws (both circumferential and axial) of a partial depth; these flaw cases are used to bound the effects of multiple crack initiations.
- The handling loads reported in design SARs are assumed to result entirely in axial stress; the entire loaded canister mass is conservatively used to calculate handling loads at the crack location. This assumption is used to simplify the calculation.

---

<sup>1</sup> The amount of time a hypothetical puddle affects the AH within a canister is inversely proportional to how much it raises the AH. Assuming the puddle affects  $\frac{1}{2}$  of the airflow through the overpack (i.e. adds humidity to  $0.15 \text{ m}^3/\text{s}$  of air), a puddle raising the AH by  $2 \text{ g}/\text{m}^3$  (values of  $< 20 \text{ g}/\text{m}^3$  are typical of atmospheric conditions) dries out at a rate of  $3.06 \times 10^{-7} \text{ m}^3/\text{s}$  (1.1 L/hr). Frequent ingress of large volumes of water would be required to change the interior climate of the canister relative to ambient on a time scale that affects CISC growth. Puddles which persist but are not refreshed by large volumes of water are not evaporating rapidly enough to affect the AH.

- The loading cases of normal internal pressure and handling are considered appropriate for these calculations because they represent the most common and routine conditions the canister may experience during storage or retrieval. Analysis with accident internal pressures provide a severe case with crack opening loads that bound the conditions that flawed canisters may reasonably experience during storage.

### **2.2.2 Gas Leakage**

The flow rate of gas through a through-wall crack is relevant in determining the timescales for the release of any internal pressure and the ingress of air into the canister.

#### **Inputs**

- Canister internal pressures from design SARs are used for leak rate calculations.
- Pressure losses along the crack depth are modeled using Appendix D of EPRI 1011820 [9].
- Hourly climate data from NOAA monitoring sites (ambient pressure and temperature) [7] are used as inputs in some of the air ingress model cases.

#### **Assumptions**

- Residual stresses due to welding are assumed to contribute to the crack opening of short flaws in or near welds, and they are applied as membrane loads in the crack opening calculation for short flaws. It is noted that, consistent with ASME Code analysis methods for ductile materials, residual stresses are not included in the ASME Code evaluation of critical flaw sizes.
- As noted in Section 2.1, flaws will tend to be limited in length by the extent of tensile welding residual stress perpendicular to the weld cross section. This tensile region has been estimated to extend about four times the wall thickness on each side of the weld centerline. Flaw lengths used for some of the crack opening cases take into account this extent of tensile stress, but larger flaw length cases are considered as sensitivity studies.
- The crack opening area is assumed to be elliptical for the purposes of determining crack opening displacement. The edges of through-wall flaws are assumed to have a radial orientation (i.e. a rectangular crack shape is assumed for crack opening calculations rather than a trapezoidal one).
- Leakage through the crack is assumed to be subject to laminar viscous losses and a tortuosity pressure loss term. This approach combines those of References [9] and [10].
- The internal pressure at the time of pressure boundary penetration is assumed to be the design normal condition value. This assumption is conservative with regard to the maximum leak rate but would over-estimate the time taken for pressure equilibration. The timescale for pressure equilibration is short relative to those of crack growth and air ingress, so this effect is not significant.
- The air ingress model is intended to provide approximate time frames for air ingress based on the mechanical behavior of the canister and does not model the chemical reactions that occur within the canister. For the intended purpose, this simplification is appropriate.
- For leakage calculations, an assumed value of 150°C (with external atmospheric conditions of 25°C and 101 kPa) is used for the average internal gas temperature based on interpretation of CFD results [11]. For ingress calculations, the internal gas temperature is 125°C hotter than the external atmospheric temperature (i.e., the same offset temperature from ambient as

in the leakage calculation). The effect of this assumption is evaluated by sensitivity cases with higher and lower internal gas temperatures and is shown to be much less important than the flow path (i.e. crack) geometry.

- Based on the sensitivity case results mentioned above, the change in internal gas temperature due to a loss of helium backfill and ingress of air are not expected to change the leak rate calculation results enough to justify adding the model complexity associated with those effects.
- Perfect mixing of helium and air is assumed within the canister such that the helium mole fraction of gas exiting the canister is the same as the average within the canister.

### **2.3 Thermal Analysis Data**

Data from canister thermal analyses are used to inform both the flaw growth and flaw tolerance assessments, but the results are presented as a function of temperature to avoid dependence on the thermal characteristics of a particular DCSS design. Calculations of decay heat are used only to model the proportional change in surface temperature over time. Consequently, the results of this assessment are weakly dependent on the inputs and assumptions within this subsection.

#### **Inputs**

- Decay heat modeling is calculated as the sum of individual fuel assembly decay heats using Appendix C of SAND87-2909 [12].
- Surface temperature distributions for horizontal canisters are provided in References [13], [11], and [14].
- Surface temperature distributions for vertical canisters are provided in References [15], [16], and [17].

#### **Assumptions**

- The canister surface temperature at a given location is assumed to be an offset from the ambient temperature at a given canister power, an approach which Table 3-4 of Reference [16] supports. The canister power—which is proportional to the offset from ambient temperature—is modeled to vary with time as shown in Figure 3-11.
- The canister surface temperature is assumed to track the fluctuations in ambient temperature. To account for thermal inertia effects of the canister internals, the 6-hour moving average of the ambient temperature is used in calculating the surface temperature.

The calculation of the change in canister temperature versus time is based on fuel assembly loadings that give reasonable decay heat curves, considering the limits in DCSS SARs. The positioning of different power fuel assemblies within the basket and the differences in axial burnup among fuel loads are not modeled. Only the change in the temperature offset versus ambient (i.e. the long-term change in temperature at a given canister surface) is dependent on the fuel characteristics. The crack growth assessment results vary only slightly for fuel loadings with different enrichment, ages at loading, and burnups. Consequently, consideration of specific assembly positioning is unimportant, and results are only presented for a single assumed fuel load.

# 3

## CRACK GROWTH MODELING

This section describes modeling performed to calculate, using conservative methodology, the time required for a previously initiated flaw in the pressure boundary of the canister to grow through-wall. The flaw growth calculations are performed using a CGR equation developed from available data. The flaw growth assessment uses the CGR equation developed and parameters based on available data to predict the propagation of chloride-induced stress corrosion cracking through the shell of the canister. The flaw growth calculations consider the effect of temperature on CGR as well as the effect of time of wetness. The timeframes calculated in this section do not consider the time required to develop conditions leading to crack initiation, which are expected to be substantial.

### 3.1 Expected Flaw Growth Characteristics

Flaw growth in this assessment is modeled as CISCC propagation through the stainless steel canister shell in regions of tensile stress, such as in the vicinity of canister shell welds. The approach to modeling the through-wall growth of flaws in the stainless steel canisters is based on the findings of the FMEA [1] and literature review [2] associated with this effort and is supported by prior EPRI literature reviews on CISCC [9] and ODSCC [18]:

- The shell and associated welds are judged to be of greater susceptibility than the canister lids since the lids are 3-18 times thicker than the shell and typically have redundancy in areas with significant tensile residual stresses.
- SCC growth is expected to occur near welds due to the presence of elevated tensile through-wall residual stress conditions and a more susceptible material condition. The weld locations for typical canister geometry are depicted in Figure 3-2. Weld metal appears to be less susceptible than adjacent base metal in laboratory experiments and OE; this may be due to the presence of delta ferrite [4]. Finite element analyses indicate that cracking most likely would be transverse to the weld bead direction and that the tensile stresses decay rapidly with distance from the weld centerline. This stress state would promote short through-wall cracks oriented transverse to the weld direction within a few wall-thicknesses on either side of the weld, as was seen in recent CISCC testing of welded plate specimens [19].
- The CGR is independent of flaw orientation and aspect ratio. The main factor which changes based on crack morphology is the calculation of the stress intensity factor, other factors which apply based on local conditions are independent of orientation. The insensitivity of crack growth rate to the stress intensity factor in available literature for atmospheric CISCC, particularly Reference [5], eliminates the importance of flaw morphology on CGR.
- CISCC flaw growth is contextualized using a semi-elliptical planar flaw geometry, as shown in Figure 3-1, with propagation in length at each surface tip and in depth at the flaw center. In the figure,  $a$  and  $c$  are the crack depth and half-length, respectively, and the principal stress is normal to the page. The lack of CGR dependence on a crack-tip  $K_I$  in available data greatly reduces the importance of part-depth flaw morphology. While CISCC frequently results in branched flaws, flaw growth typically occurs with a predominant orientation perpendicular to that of the maximum principal stress.

- Based on the results of two test programs that continuously monitored crack depth ([20] and [6]), a two-phase crack growth model is applied which reduces the crack growth rate once the crack propagates beyond a prescribed depth. An example of the direct current potential drop (DCPD) data showing this two-phase growth is shown in Figure 3-3. The anticipated mechanism for a reduction in propagation rate with depth is a limiting of the corrosion current that can be supplied by the cathodic area on the material surface as the crack tip—the anode—moves further away, thereby increasing the ohmic resistance. Immersion testing has shown that the crack growth rate is proportional to the corrosion current between the anode and cathode locations and that the current is strongly affected by the rate of the oxygen reduction reaction at the cathode [21]. Smaller and discontinuous deliquescent films (at lower salt areal densities and lower humidity) limit the cathodic area able to drive the localized corrosion and produce less aggressive environments ([22], [23], and [24]).
- The compressive residual forming stresses present on the OD of the canister shell [1] and low operational pressure stresses reduce the likelihood of SCC occurring in material distant from the welds.
- A wide range of surface temperatures exists on the canister outer surface, and the temperatures decrease over time. Therefore, it is difficult to ascribe a single temperature profile to a given canister design and heat loading. Instead, an initial surface temperature is chosen (from within a representative range) for the crack growth calculations and is decreased with the canister thermal power.
- For material of thicknesses relevant to the canister pressure boundary, through-wall penetration is expected to occur due to SCC rather than pitting. Pitting is frequently a precursor to SCC, but pitting is not expected to produce leaks in the absence of SCC based on industry experience of leaks caused by atmospheric corrosion. Pit penetration rates typically decrease over time for atmospheric exposure, and time-averaged pitting penetration rates of about 5.5  $\mu\text{m}/\text{yr}$  were reported for 26 year exposure testing 25 m from the ocean at Kure Beach, NC [2].
- The occurrence of CISCC within crevices and pits is not expected to substantially affect the propagation rate of the macro-scale SCC crack. Comparing the results of single and double U-bend testing, NUREG/CR-7030 stated that “crevices did not appear to preferentially foster corrosion” [25] apparently because the deposited salt was not wicked into the crevice.

A common conceptualization is that crack initiation from localized corrosion occurs once conditions evolve (e.g., by increased  $K_I$  caused by a pit) such that crack growth is more rapid than the blunt dissolution by localized corrosion [26]. Once the crack has initiated, crack growth progresses more rapidly than the localized corrosion, and it is expected that the influence of the pit or crevice on the crack environment will decrease because the crack itself is also an isolated electrochemical cell [3].

Since the growth is expected to be limited by the available cathodic area caused by the finite size of the deliquescent film on the canister surface ([27] and [28]), any active dissolution within the crevice would tend to compete with the propagating crack for cathodic capacity. Conversely, if the pit or crevice growth slows or arrests, the concentrating effect on the occluded solution would be moderated. Testing of immersed specimens indicated that the electrical resistivity of the crack increases as it grows [29]. Stress concentration effects of the pit or crevice geometry would decrease as the crack tip propagates away from the localized corrosion.

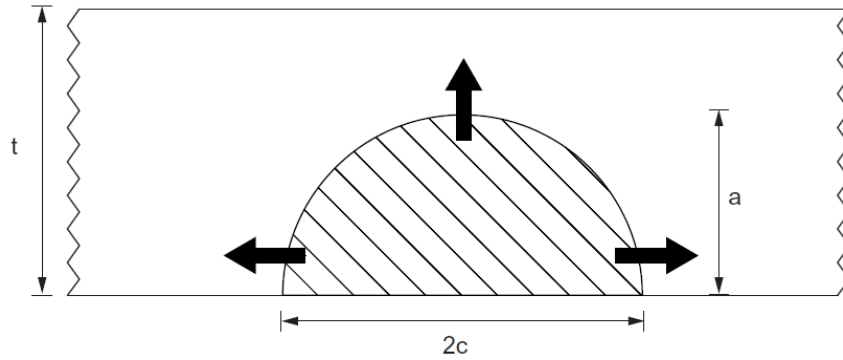


**Figure 3-1**  
**Diagram of Idealized Part-Depth Flaw Growth (Tensile Stress is Normal to the Page)**

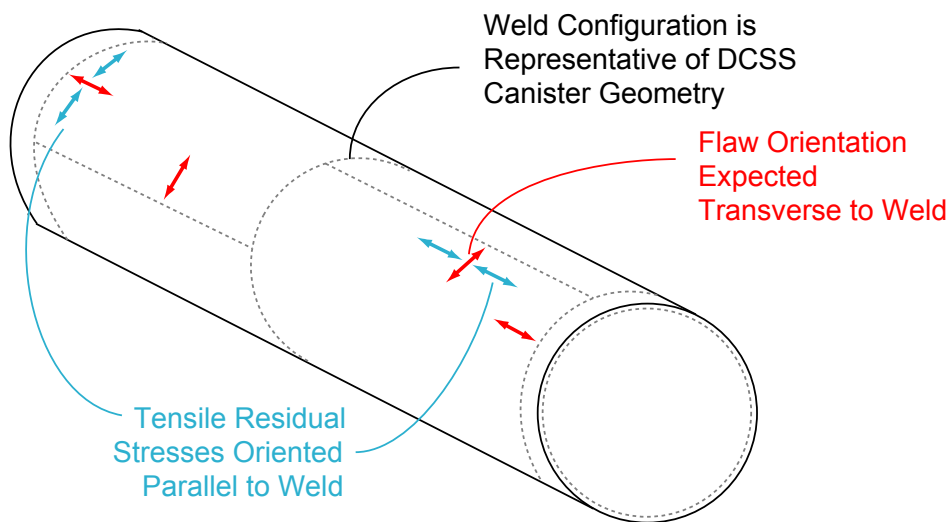


**Figure 3-2**  
**Representative Canister Weld Configuration**

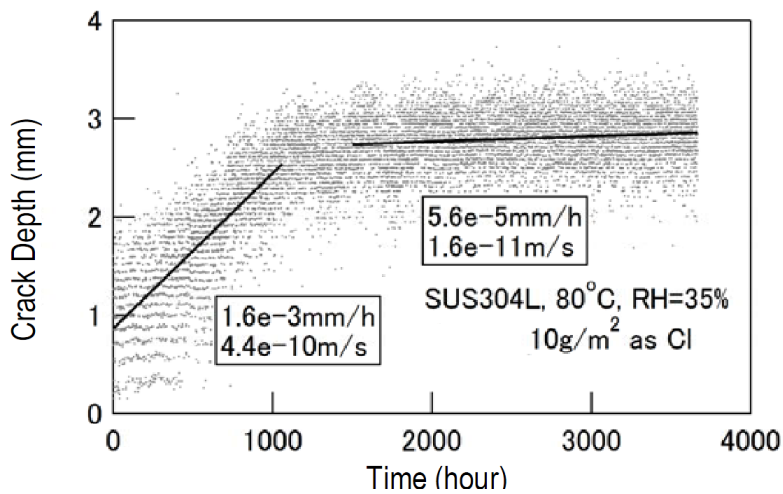


**Figure 3-3**  
**DCPD Data Showing Two-Phase Growth (Reprinted from [30])**

## **3.2 Chloride-Induced SCC Flaw Growth Model**

The flaw growth model is summarized in this section and described in more detail in Section A.2. A review of literature [2] did not identify an established crack growth relation for CISCC at temperatures below 100°C or in atmospheric conditions. In order to quantify the rate of atmospheric CISCC propagation, a new CGR equation is developed in this report. The CGR equation is based upon the typical form of SCC flaw propagation, such as those found in Section XI Nonmandatory Appendix C, Article C-8000, of the ASME Boiler and Pressure Vessel Code. The crack growth rate formula includes an Arrhenius relation to describe the thermal dependence and additional factors to describe other dependencies. The primary factors considered in developing the crack growth rate equation are: the stress intensity factor (see Section A.2.2.1), the material temperature (see Section A.2.2.2), the ambient humidity (see Section A.2.2.3), the chloride areal density (see Section A.2.2.4), the crack depth (see Section A.2.2.5) and the material alloy (discussed below). The available crack growth rate data are used to determine the dependence of the crack growth rate on each of these factors. These relations are used, in turn, to normalize the dataset upon which the first and second phase crack growth rate coefficients are based.

### **3.2.1 CGR Coefficient for Atmospheric CISCC**

The CGR coefficients are developed using experimental crack growth data and an assumed temperature dependency for stress corrosion cracking. The final database of CGRs used to generate the crack growth rate coefficients are narrowed to consider only data representing specimens loaded with sea salt (natural or simulated) for which a crack growth rate is measured in a way that avoids inclusion of initiation time (e.g., continuous crack measurement or a sharpened pre-crack). To model the two-phase crack growth rate observed in CRIEPI testing [30], the sets of shallow and deep growth data are analyzed separately to obtain statistically conservative first and second phase CGR coefficients, respectively.

A description of the conditions under which the data were generated and the process used to normalize the data is provided in Section A.2.2.5. After normalizing the data, statistical analysis of the data sets is performed as described in Section A.2.3 to determine statistically conservative values for the CGR parameters. The resultant distribution and adjusted data points are plotted in Figure 3-4, with key percentiles labeled. The key statistics of the fit are presented in Table 3-1.

Most of the crack growth data were obtained at 80°C; therefore, 80°C is used as the reference temperature for thermal effects. Crack growth rate data at other temperatures would be adjusted to a reference temperature of 80°C using an Arrhenius relation with a characteristic activation energy. Section A.2.2.2 describes the basis for the chosen activation energy of 40 kJ/mol and discusses the variability in activation energy among experiments. The 40 kJ/mol activation energy is at the lower end of the range of values, and it is selected to be conservative given the elevated reference temperature. The data used to determine the CGR coefficient are based on severe experimental conditions; therefore, the crack growth model results are expected to be conservative relative to typical canister conditions.

Among the data accumulated by the literature review [2], CGR data was found for both pure salts (e.g., MgCl<sub>2</sub>) as well as for sea salt. Data for pure salts are not used because sea salt is considered the best representation of marine environments, a reasonable representation for mixed chlorides present in other environments, and a conservative approach relative to NaCl. CGR data

are not inferred from data presented as crack depth and exposure time because the unspecified initiation time would affect the resultant CGR; likewise, reported CGR data that includes an unknown initiation time period are not considered. Additionally, data from atmospheric testing is not included because of significant variability and uncertainty regarding the environmental conditions, including the daytime specimen temperature [31].

References [20] and [6] reported data which meet the criteria for inclusion in the shallow cracking data set. Reference [20] contained low CGR data at 50°C that were consistent with an activation energy of 190 kJ/mol. These were conservatively omitted because they would significantly reduce the mean value. Reference [6] reported data which meet the criteria for inclusion in the deep cracking data set.

Due to the small dataset and the importance of the CGR in determining the primary result (through-wall growth time) without additional safety factors, a statistically conservative assessment is appropriate. The statistical process, described in Section A.2.3, considers the uncertainty in both the mean and the distribution of the data.<sup>2</sup> Furthermore, the use of a low activation energy in combination with a relatively high reference temperature conservatively results in higher calculated growth rates at the lower canister temperature.

**Table 3-1**  
**Statistics for the Upper Bound of the 50% Confidence Interval Log-Normal Fit to the Data at 80°C**  
**in Figure 3-4 and Figure 3-5**

Percentile	1 <sup>st</sup> Phase CGR Coefficient	2 <sup>nd</sup> Phase CGR Coefficient
5%	0.714	0.049
50%	11.0	0.33
75%	33.6	0.71
95%	168	2.19
98%	332	3.51

---

<sup>2</sup> The log-normal fit to the data is obtained using the upper limit of the 50% confidence interval on the mean, and the 95<sup>th</sup> percentile value of this revised fit is used as the CGR coefficient.

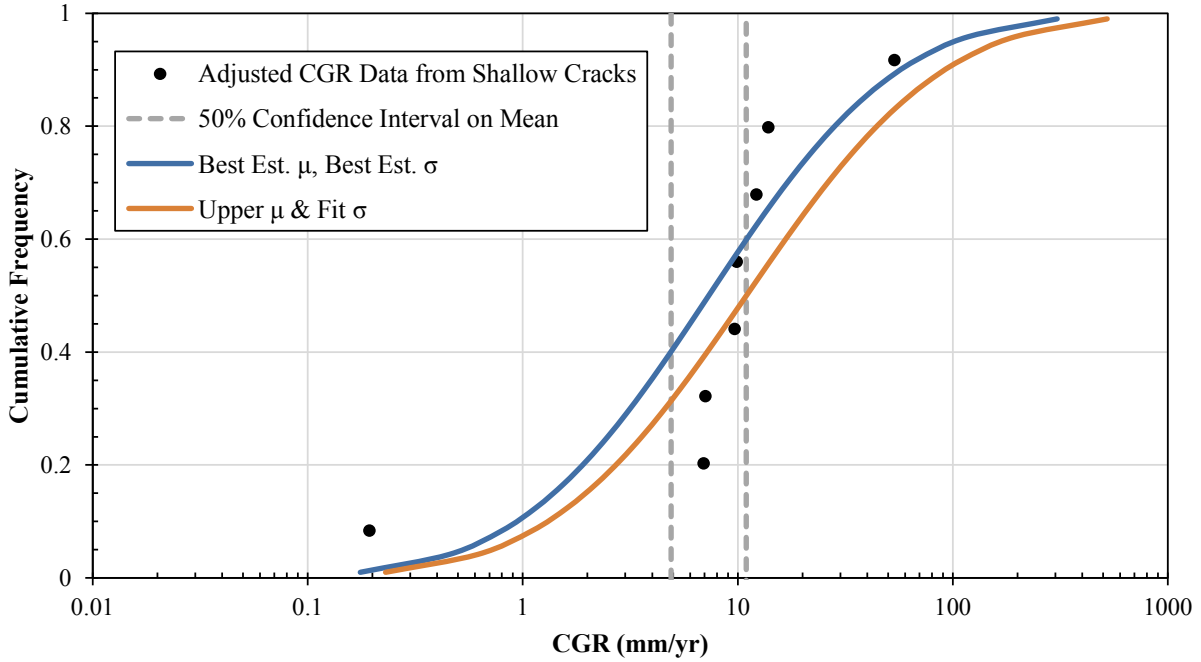


**Figure 3-4**  
**Cumulative Distribution for CISCC Experiments Reporting CGR Data for Sea Salt ([20] and [6]), in Shallow Cracks (First Phase Growth)**

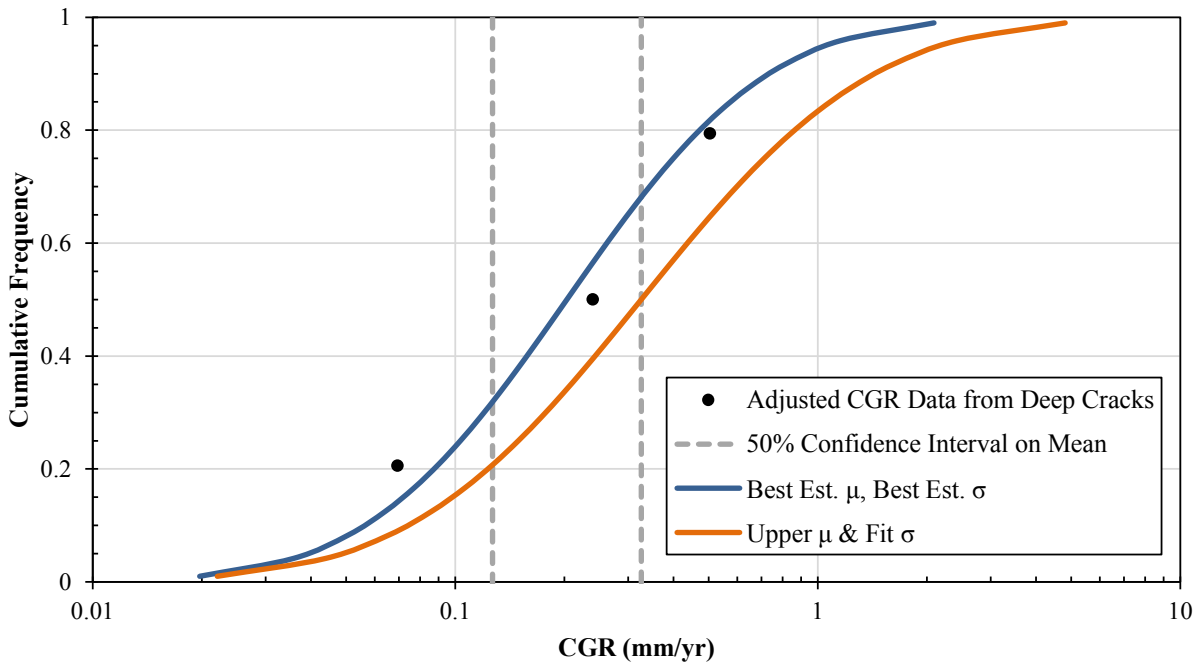


**Figure 3-5**  
**Cumulative Distribution for CISCC Experiments Reporting CGR Data for Sea Salt [6], in Deep Cracks (Second Phase Growth)**

### 3.2.2 CISCC CGR Equation

The crack growth rate formula includes a coefficient obtained by fitting a distribution to normalized data, an Arrhenius relation to describe the thermal dependence and additional factors to describe other dependencies.

As described in Section A.2.2.1, the crack growth rate model is independent of the crack tip stress intensity factor ( $K_I$ ) for tensile values. For the available data, predominately found in Reference [5], CGR data exhibit a very weak dependence on crack-tip  $K_I$ .

Since ambient humidity is naturally limited, sea salt on sufficiently hot surfaces will not deliquesce, and salt deposits on cooler surfaces will deliquesce only for a fraction of the year. For times when the salt deposited on the surface is dry, flaw growth stops due to the lack of an aqueous area to act as a cathode. The RH value where the salt is considered wetted is calculated as described in Section A.1.1; this calculated RH value is conservative relative to measured and analytical deliquescence and efflorescence data for sea salt. Both the canister surface temperature (a function of the ambient temperature and thermal power) and the absolute humidity vary throughout the year at a given location. With both the Arrhenius temperature factor and the humidity factor dependent on ambient temperature, the hourly climate data is used to calculate the crack propagation over time, as noted in Section A.2.2.3, rather than evaluating the CGR over larger time steps that neglect important diurnal variations. This approach does not consider any beneficial evolution of deposits over time that can result from intermittent wetting of deposited chlorides (e.g., chloride volatilization and removal by displacement reactions with nitrates), as was reported in CRIEPI experiments on page A-7 of Reference [9].

As described in Section A.2.2.4, there is currently insufficient crack growth rate data to support a dependence on chloride areal density. It is noted that the CGR data used for the model were generally obtained with experiments using relatively high surface load values; i.e., about 10 g/m<sup>2</sup>.

Although Type 316 stainless steel, as well as low carbon 304L and 316LN grades, typically experience longer times to initiation and lower susceptibility to chloride-induced degradation than Type 304, the small quantity and inherent scatter of the currently available data are not sufficient to support different crack growth rates for each alloy. Accordingly, there is not a separate factor or adjustment to the CGR coefficient for the alloy type. The material condition (e.g., sensitization, cold work, etc.) and presence of other species in the aqueous layer of deliquescent brine are considered so far as they were included in the underlying data used to determine the crack growth rate coefficient. While studies of the dependence of time to initiation on material condition have been performed, no atmospheric growth rate testing was available to determine a dependence.

Using the above information and the CGR coefficients from Section 3.2.1, the crack growth rate equation for CISCC at a given point in time is modeled as follows:<sup>3</sup>

---

<sup>3</sup> Section A.2.1 provides the form of Equation 3-1 when averaged over time and the full form of the temperature and humidity dependencies as they relate to measured data.

$$\frac{da}{dt} = \begin{cases} \alpha \exp\left[-\frac{Q_g}{R}\left(\frac{1}{T} - \frac{1}{T_{ref}}\right)\right] & \text{for } RH \geq DRH \text{ and } K_1 > 0 \\ 0 & \text{for } RH < DRH \text{ or } K_1 \leq 0 \end{cases} \quad \text{Eq. 3-1}$$

where

$\frac{da}{dt}$  = crack depth growth rate

$\alpha$  = crack growth rate coefficient (mm/yr), derived in Sections A.2.2.5

=  $\begin{cases} 168 \text{ mm/yr for } a < 3.16 \text{ mm} \\ 2.2 \text{ mm/yr for } a \geq 3.16 \text{ mm} \end{cases}$  (Reference Temperature = 80°C)

$Q_g$  = crack growth activation energy (kJ/mole), see Section A.2.2.2

= 40 kJ/mole

$R$  = universal gas constant (kJ/mole/K)

= 0.008314 kJ/mole/K

$T$  = surface temperature (K), obtained by measurement or analysis using Equation A-5

$T_{ref}$  = Arrhenius reference temperature (K), see Section A.2.2.2

= 353.15 K (80°C)

$RH$  = local relative humidity at surface (%), obtained from surface temperature and ambient absolute humidity using Equation A-6

$DRH$  = deliquescent relative humidity of deposited chloride salts (%), in this work Equation A-1 of Section A.1.1 is used

A visual depiction of the CGR calculation steps over a seven-day period is provided in Figure 3-6 and Figure 3-7. The figures depict results for a surface location which is, at that time, 20°C hotter than ambient and subject to the Camp Pendleton, CA environmental conditions. To account for thermal inertia of the fuel and canister internals, the surface temperature follows the 6 hour moving average of the ambient temperature. Gaps in the growth rate occur when the RH is lower than the DRH; i.e., the deposits are dry. Section A.1.1 contains further discussion of the applicability of a RH threshold.

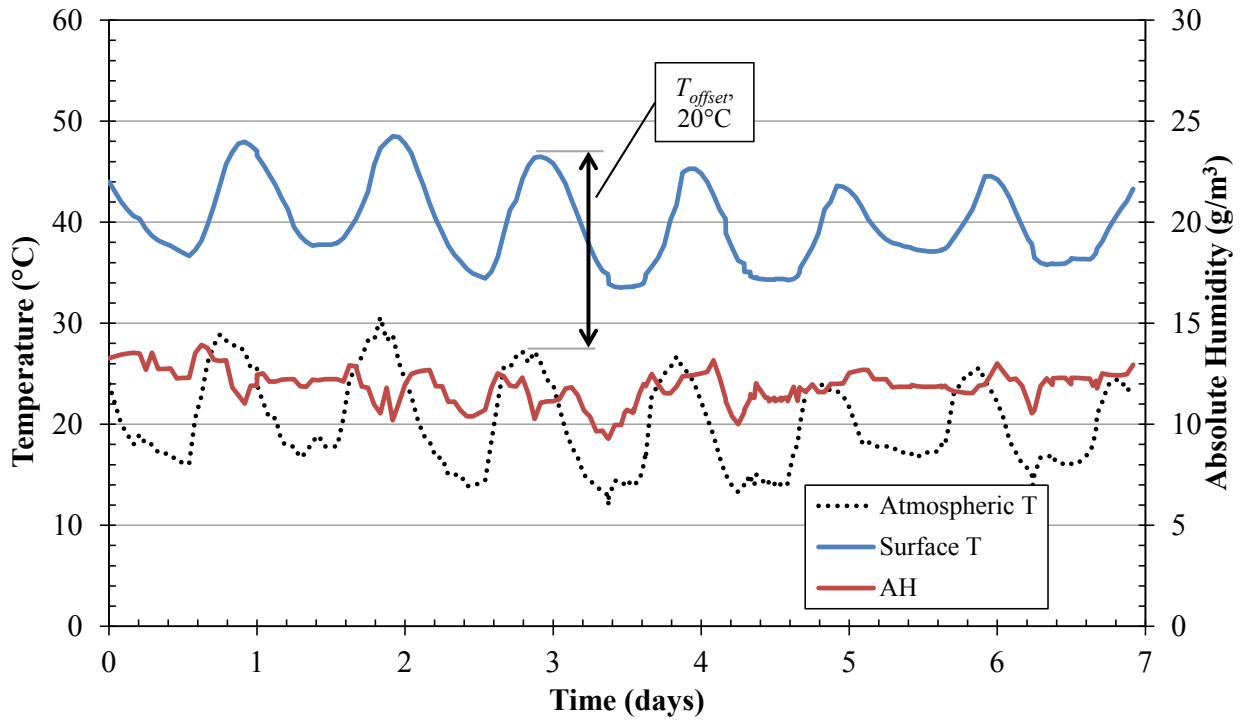


**Figure 3-6**  
**Canister Surface Temperature Calculated from the Atmospheric Temperature, Plotted with the Absolute Humidity, First Week of August 2011, Camp Pendleton, CA**

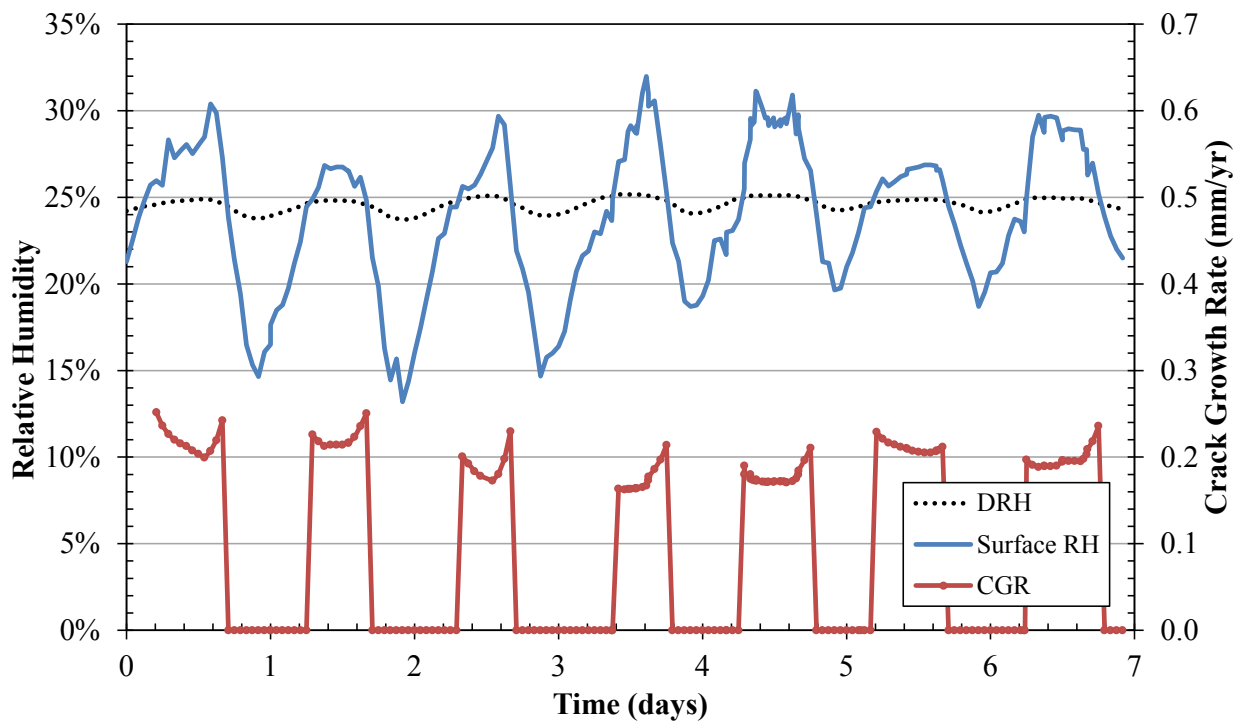


**Figure 3-7**  
**Plot of Surface RH and DRH for Conditions in Figure 3-6 and the Resultant CGR**

### 3.3 Model Results

This section summarizes key results stemming from the application of the crack growth rate equation defined by Equation 3-1 to locations characteristic of the climate at sites across the U.S. and for parameters typical of DCSS canisters in service.

Since the current data do not support a substantial dependence of crack growth rate on  $K_I$ , growth of cracks at locations in the canister where tensile stresses are maintained through-wall are treated identically. Consequently, the only difference in modeled CGR among different locations on the canister is the material temperature. Welds run along the axial length and around the girth of the canister shell, and there are a wide range of temperatures present on the canister surface at a given point in time. Therefore, a range of potential surface temperatures are present at locations that may be susceptible to CISC initiation and growth.

Two primary sets of analyses are performed when calculating crack growth: (1) the environmental factors are evaluated for different climatic regions using ambient temperature and absolute humidity data, and (2) crack growth is modeled starting at a given surface temperature, which then decreases as the thermal output of the fuel decays with time.

#### 3.3.1 Crack Growth Rates for Various Climates

The crack growth expected for a given climate and for a canister location at a given temperature is predicted for climates relevant to potential chloride-induced SCC at ISFSIs. Locations and key information for the climate monitoring stations considered are summarized in Table 3-2. As shown in Table 3-2, an AH of 30 g/m<sup>3</sup> is bounding for atmospheric conditions, and an AH less than 15 g/m<sup>3</sup> occurs for a large portion of the year. Figure 3-8 shows that the peak effective CGR varies by a factor of more than two for different climates and is very low in arid locations. It is noted that this difference would increase if an activation energy higher than 40 kJ/mol is used.

The climates chosen include a Pacific coast location, South Atlantic coast locations, a Mid-Atlantic coast location, a South West arid location, and a Mid-West location far from the ocean. For each location, hourly climate data are obtained over an entire calendar year and are filtered to eliminate spurious values, as described in Section A.1.2. As mentioned in Section 2.1.3, rare weather events (e.g., hurricanes) do not have a substantial effect on the timescale of flaw propagation, and the ingress of rainwater through vents will not substantively affect the AH within the overpack relative to ambient. Variation in climate for different years is a similarly small factor, as shown in a sensitivity case in Section 3.3.2. The evaluated environmental data are taken from atmospheric monitoring stations, which is considered an accurate first order representation of the environment at the nearby ISFSI location for the scope and scale of the calculations performed.

The environmental factor (combined effect of temperature and humidity factors,  $f_{T/H}$ ) is evaluated as a function of the difference between the canister surface temperature and the ambient temperature (e.g., a location on the canister that is 55°C when the ambient temperature is 20°C would be evaluated by adding 35°C to the ambient temperature data). The average effect of climate over a year for a surface at a given temperature offset is presented in Figure 3-8, accounting for the hourly variation in ambient temperature and absolute humidity over an entire year. To account for the thermal inertia of the canister internals, a roughly six-hour moving average of the temperature is used.

As previously noted, the canister surface temperature is established by a calculated offset relative to the ambient temperature. Figure 3-8 demonstrates the competition between increased exposure to deliquescent conditions as the surface temperature decreases and thermally reduced corrosion kinetics; i.e., lower temperatures result in more frequent crack growth due to deliquescence but at a slower rate during those times. The model predicts that each environment considered will have a specific surface temperature at which a maximum crack growth rate will occur. Figure 3-8 also demonstrates that canister local surface temperatures that are greater than about 30°C above ambient temperature are not subject to crack growth (due to lack of deliquescence).

**Table 3-2**  
**Locations and Key Information for Climate Data from Reference [7] Analyzed in this Technical Update**

Location	USAF Identifier	Start Date	End Date	Max AH (g/m <sup>3</sup> )	Mean AH (g/m <sup>3</sup> )	Mean T (°C)
Camp Pendleton, CA	722926	1/1/2011	1/1/2012	15.5	9.1	15.0
Joliet, IL	725345	1/1/2011	1/1/2012	25.4	8.1	10.6
Homestead, FL	722026	1/1/2011	1/1/2012	26.1	17.7	24.5
Patuxent, MD	724040	1/1/2011	1/1/2012	25.7	10.0	15.2
Chester, CT	720545	1/1/2011	1/1/2012	23.6	8.7	11.4
Witham Field, FL	722189	1/1/2011	1/1/2012	25.6	16.2	24.2
Buckeye, AZ	720644	1/1/2011	1/1/2012	23.0	5.8	21.7

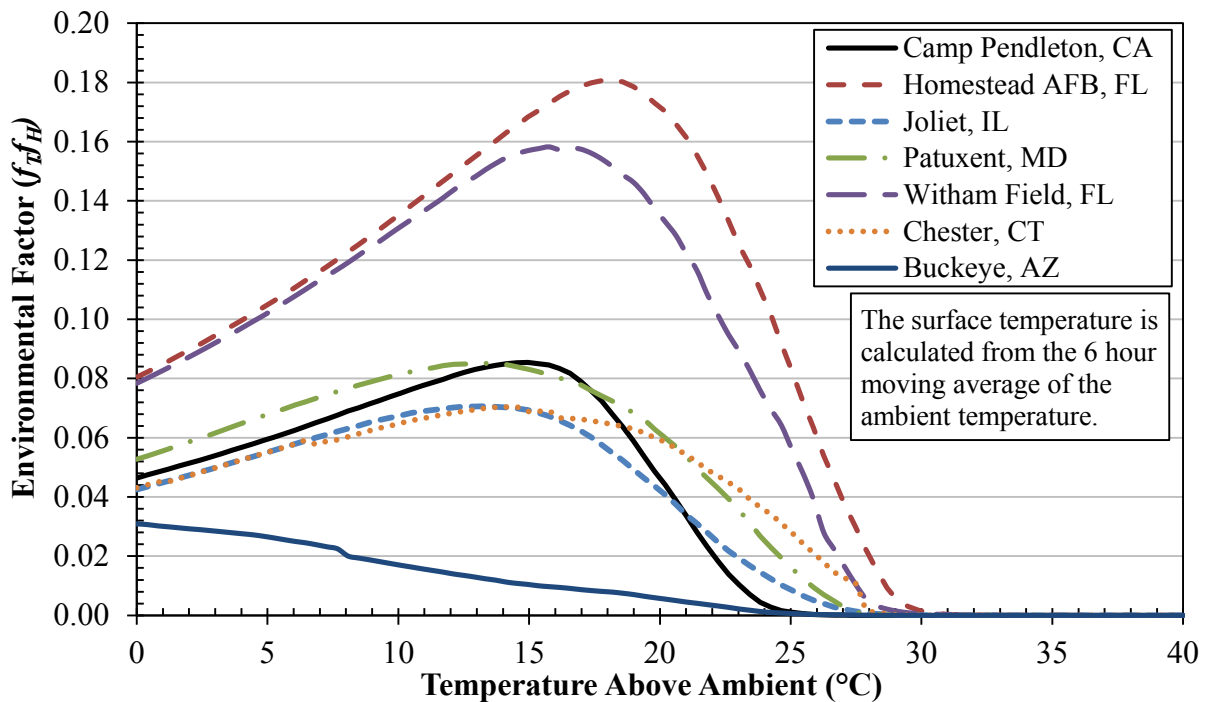


**Figure 3-8**  
**Average of the Environmental Factor on CGR ( $f_{RH}$ ) Based on One Year of Hourly Climate Data for Different Locations**

### 3.3.2 Flaw Growth Results

The flaw growth analysis results presented in Table 3-3 and Table 3-4 provide examples of the time required for a crack to propagate through a canister shell with a thickness of a half-inch (13 mm). Through-wall growth for canister shells of 15.9 mm (0.625 inch) takes approximately 30% longer, as shown by case 15. Since the flaw growth relation is independent of crack tip stress intensity factor, the orientation of the flaw and the through-wall stress profile do not affect the growth rate, and the results near seam, girth and shell-to-lid welds would be identical.

As noted previously, the CGR modeling is based on the crack growth coefficient for the 95<sup>th</sup> percentile of the log-normal fit for the 50% confidence interval mean and a fitted standard deviation, shown in Figure 3-4 and Figure 3-5. The use of such a statistically conservative value is appropriate because of the uncertainty associated with small data sets and because through-wall penetration is a highly significant outcome.

During the crack growth calculation, the canister surface temperature decreases with increasing storage time in a manner proportional to the modeled decay power, shown in Figure 3-11 for a mixture of burnups. The temperature decay is modeled by assuming a linear dependence of surface temperature with fuel assembly decay power, as calculated in Section A.3.1. Additionally, the temperature is modeled to decay proportional to power for a fuel loading that starts at 12.2 kW about a decade after discharge from the reactor. Internal evaluations show that the assumed fuel parameters used to generate the power curve do not have a substantial effect on the crack propagation time.

Since the canister surface temperature at a given location decreases with time, the temperature used as a starting point for the flaw growth calculation will influence the final result. The cases in Table 3-3 vary the initial temperature of the flaw growth calculation to which the decay curve in Figure 3-11 is applied, with cases for canister surface temperatures at 35°C, 25°C, and 15°C above ambient. Two different environments are considered in these sensitivity studies: a South East environment (cases 1 to 3) and a West Coast environment (cases 4 to 6). The crack growth as a function of time is shown in Figure 3-9 for cases 1 to 3 and Figure 3-10 for cases 4 to 6. As shown in these figures, the crack propagation in the first phase growth regime is very rapid and accounts for a year's worth of propagation time. Because cases 1 and 4 start at temperatures hot enough to preclude deliquescence, no growth occurs for the first few years. This is comparable to starting at +35°C on Figure 3-8, then moving to the left along the x-axis as the canister cools.

Table 3-4 provides sensitivity cases that evaluate the effect of various assumptions and the relative importance of parameters used to model flaw propagation. The sensitivity cases are variations on case 2 and case 5, which evaluate South East and West Coast environments, respectively, at a temperature 25°C above ambient. Analysis case 7 uses the same parameters as case 2, but uses the environmental data from a different monitoring site in the southeast U.S. as an input; the crack growth is slower using this third location's data. Case 8 evaluates the effect of using 4 years (1/1/2008 to 12/31/2011) of climate data instead of the single year; the difference is minor. Analysis case 9 uses the 95<sup>th</sup> percentile value of the log-normal distribution that is the best-fit to the CGR coefficient datasets rather than the default statistical approach; the crack growth in this case is considerably slower. Cases 10 through 13 comprise a sensitivity study of changes to the activation energy used in calculating the temperature-adjusted crack growth rate. Cases 10 and 12 result in penetration times about two-thirds as long as their respective base cases

while cases 11 and 13 result in penetration times about five times longer their respective base cases. Case 14 considers the effect of a transition point between the shallow crack growth and deep crack growth phases that is twice the base case; relative to the base case, the time to reach through wall is reduced by about 30%. Case 15 considers a canister wall thickness of 15.9 mm (0.625 inch); relative to the base case, the time to reach through wall for this case is increased by about 40%. The 7 percentage point DRH offset, explained in Section A.1.1, is varied by 3 points in cases 16 through 18. Varying the DRH offset by 3 points shows that the results are less sensitive to increases in the offset than reductions; i.e., choosing a more conservative offset does not change the results substantially.

**Table 3-3  
Crack Growth Analysis Results for Varying Climates and Initial Surface Temperature Offsets**

<b>Case #</b>	<b>Case</b>	<b>Surface Temp. at Crack Initiation</b>	<b>Source of Climate Data</b>	<b>Time to Grow 50% TW (Note 1) (yr)</b>	<b>Time to Grow 75% TW (yr)</b>	<b>Time to Grow TW (yr)</b>
1	South East	Ambient +35°C	Homestead AFB	24.4	32.9	41.0
2	South East	Ambient +25°C	Homestead AFB	10.1	18.2	26.5
3	South East	Ambient +15°C	Homestead AFB	9.4	19.7	30.9
4	West Coast	Ambient +35°C	Camp Pendleton	45.7	62.9	81.3
5	West Coast	Ambient +25°C	Camp Pendleton	26.2	43.8	63.2
6	West Coast	Ambient +15°C	Camp Pendleton	18.2	38.7	61.7

Note 1: Canister shell thickness is 12.7 mm (0.500 inch).

**Table 3-4  
Crack Growth Analysis Sensitivity Cases**

Case #	Case	Surface Temp. at Crack Initiation	Source of Climate Data	Time to Grow 50% TW (Note 1) (yr)	Time to Grow 75% TW (yr)	Time to Grow TW (yr)
7	Second South East Location	Ambient +25°C	Witham Field	13.1	22.8	32.3
8	Climate Data Over 4 Year Period (2008-2011)		Homestead AFB	10.4	18.7	27.3
9	95 <sup>th</sup> Percentile $\alpha$ for Best Fit Log-Normal Dist.		Homestead AFB	25.0	51.8	84.3
10	Activation Energy of 30 kJ/mol		Homestead AFB	7.5	13.2	18.6
11	Activation Energy of 80 kJ/mol		Homestead AFB	48.0	>120	>120
12	Activation Energy of 30 kJ/mol		Camp Pendleton	19.2	29.1	38.9
13	Activation Energy of 80 kJ/mol		Camp Pendleton	>120	>120	>120
14	Deeper Transition at 6 mm		Homestead AFB	1.7	11.0	19.1
15	Shell Thickness of 15.9 mm		Homestead AFB	14.2	24.3	35.6
16	DRH Offset = 10%		Homestead AFB	7.2	14.4	22.1
17	DRH Offset = 4%		Homestead AFB	14.9	24.3	33.5
18	DRH Offset = 4%		Camp Pendleton	35.1	54.5	75.6

Note 1: Canister shell thickness is 12.7 mm (0.500 inch) for all cases except for case 15.

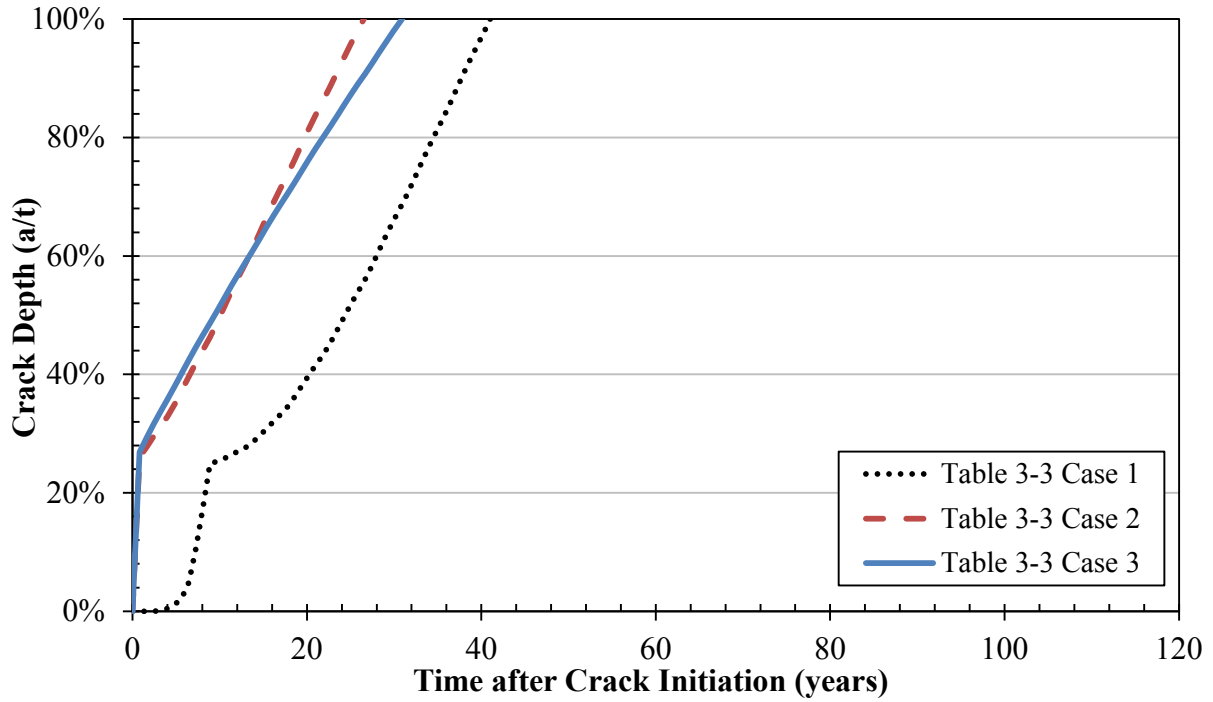


**Figure 3-9**  
Crack Depth vs. Time for South East (Homestead AFB, FL) Cases in Table 3-3

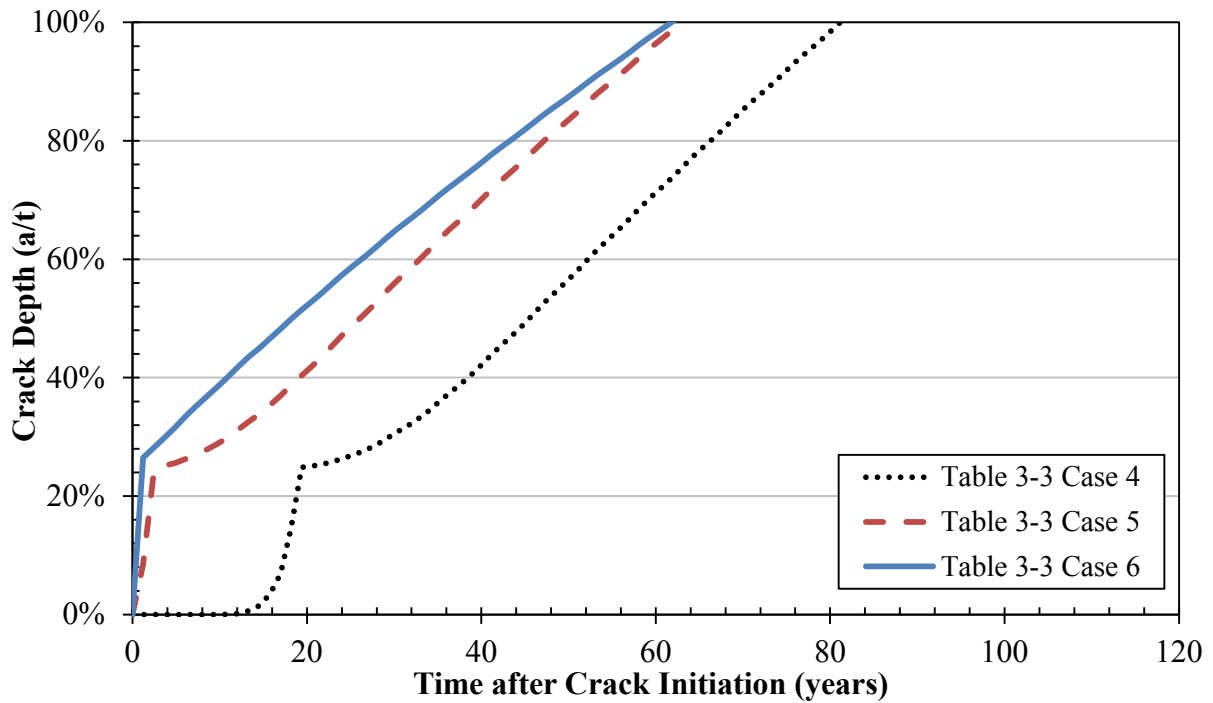


**Figure 3-10**  
Crack Depth vs. Time for West Coast (Camp Pendleton, CA) Cases in Table 3-3

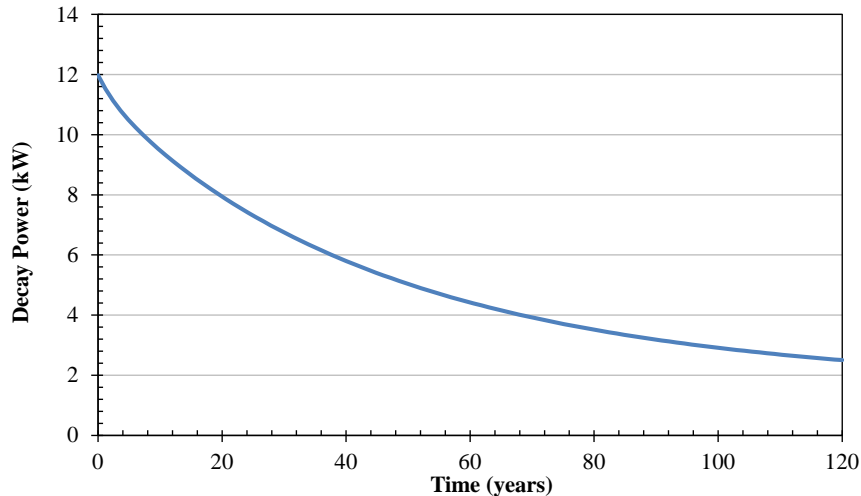


**Figure 3-11**  
**Decay Power Curve for Cases in Table 3-3 and Table 3-4 (Generated for 10 Assemblies of 40 GWd/MTHM After Wet Storage for 10 yr and 14 Assemblies of 30 GWd/MTHM After Wet Storage for 15 yr)**

### 3.3.3 Comparison with Relevant Operating Experience

Operating experience has shown that CISCC can occur due to exposure to marine atmospheric conditions at plants near the seashore. In general, through-wall cracking has typically been identified after a service life of 15-25 years and involves components less than 7.6 mm (0.3 inch) thick. Specific examples include:

- 16 years after commissioning, leaks due to CISCC were discovered in two pieces of 0.25 inch (6.35 mm) thick piping in the emergency core cooling system (ECCS) near the refueling water storage tank (RWST) at St. Lucie Unit 2 [32]. The component operated at low temperature and operating stress (30 psig and 120°F, 207 kPa and 49°C). The piping was Class 1 Type 304 piping and the most severe indications occurred in the vicinity of the weld. The leaking piping was located within the RWST trench. Through-wall leaks were not discovered on similar, thicker piping in the same location.
- After being in service for 25 years, leaks were identified in a similar location at San Onofre Units 2 and 3 (in the ECCS suction piping and the piping from the RWST to the charging pumps) [33]. The cracking occurred in the HAZ of the Type 304 components' welds for both NPS 6 SCH 10 and NPS 24 SCH 10 piping (0.13 inch (3.3 mm) and 0.25 inch (6.35 mm) thick). At least one of the leaking pipes was located within a tunnel exposed to the atmosphere.

While the operating experience demonstrates that the growth times calculated in this assessment are reasonable, key differences exist between the environment of ECCS piping and storage tanks—for which CISCC has been observed—and that of canisters. Ambient temperature components are exposed to humidities substantially above the DRH, while canisters would predominantly be exposed to humidities below or just above the DRH. For exposed piping, solar heating can raise the temperature significantly while at nighttime it can be exposed to high humidity and condensation. These dynamic differences in environment and the unknown time for chloride accumulation and flaw initiation preclude benchmarking the model to most relevant OE.

# 4

## FLAW TOLERANCE ASSESSMENT

The flaw tolerance assessment for stainless steel DCSS canisters is divided into two main sections: the first section considers the structural tolerance of the canister shell to flaws, and the second section considers the loss of the pressure boundary and the ingress of an oxidizing atmosphere.

### 4.1 Flaw Size Tolerance

This section evaluates the critical flaw size for the canister under different loading conditions.

#### 4.1.1 Load Cases

The various cases of the critical flaw size analysis consider stresses due to internal pressure and handling loads, as reported in Table 4-1 for the various canister designs. The main cases considered are a normal “handling” scenario (normal internal pressure with handling/lifting load) and an accident load scenario (accident internal pressure with normal handling/lifting load).<sup>4</sup> Including the handling load with these cases is conservative relative to the typical on-pad storage conditions where only internal pressure loads are experienced.

As the decay power of a canister decreases with time, the internal temperature and pressure will also decrease; however, design pressures are used to bound the actual pressures experienced within a canister over its entire life. If this conservative assumption were replaced with a specific canister’s pressure to evaluate its flaw tolerance after decades in storage, the pressure would be much lower than the design basis pressure.<sup>5</sup> The scope of this assessment is limited to the time of canister storage, so canister transportation and its associated loads are not considered.

---

<sup>4</sup> SARs consider design basis accidents that result in tip-over, canister drop, blocked inlet vents, and other severe events; the design accident pressure is used because it bounds all thermal accidents and, as a primary load, provides reasonably bounding conditions for large flaw sizes.

<sup>5</sup> For a hypothetical initial average gas temperature of 250°C, the absolute pressure will drop by 40% as the average gas temperature reaches 50°C.

**Table 4-1  
Load Cases Considered in this Section (Note 2)**

Case	Geometry	Shell Thickness (mm)	Design Internal Pressure [MPa(psig)]	Loaded Canister Mass [kg(kips)]	Axial Handling Load or Acceleration
Normal NUHOMS	NUHOMS 32PT	12.7	0.10 (15)	47500 (104.7)	27200 kg (60 kips)
Normal HI-STORM	HI-STORM MPC-32	12.7	0.69 (100)	40800 (90)	1.15g
Normal UMS	UMS-24	15.9	0.10 (15)	34500 (76)	1.1g
Normal MAGNASTOR	MAGNASTOR 37	12.7	0.76 (110)	46500 (102.5)	1.1g
Accident NUHOMS	NUHOMS 32PT	12.7	0.72 (105)	47500 (104.7)	36300 kg (80 kips)
Accident HI-STORM	HI-STORM MPC-32	12.7	1.38 (200)	40800 (90)	Normal case values (Note 1)
Accident UMS	UMS-24	15.9	0.45 (65)	34500 (76)	
Accident MAGNASTOR	MAGNASTOR 37	12.7	1.72 (250)	46500 (102.5)	

**Notes:**

1. Accident handling loads are not provided by the SARs for these DCSS because other design basis accident scenarios (e.g. vertical drops) are bounding. A combination of accident pressure and normal handling is evaluated here to provide a severe accident case using global loads specified in the designs' SAR.
2. The values in this table are taken from the design basis SARs for each design ([34], [35], [36], and [37]).

**4.1.2 Critical Flaw Size and Net Section Collapse**

The critical flaw size under normal and accident level primary canister loads was calculated using the load conditions specified in Table 4-1. The critical flaw lengths for through-wall axial and circumferential flaws were calculated, as well as the critical flaw depth for arbitrarily long flaws in the axial and circumferential directions (referred to as part-depth (PD) flaw cases). The part-depth flaw geometry is used to bound the hypothetical case of multiple initiated flaws in close proximity to one another.

All flaw size calculations were performed using the limit load criteria defined in Article C-5000 of Appendix C of the 2013 ASME Boiler and Pressure Vessel Code Section XI (plastic fracture using limit load). The selection of Article C-5000 is based on the flowchart Figure C-4210-1, which specifies Article C-5000 for flaws in austenitic material base metal.

Because the flaws are hypothetical and are not being evaluated to remain in service, no service level safety factor was applied to the calculations.

The following flaw type evaluations were performed as follows:

- Equation (8) in C-5430 is used to evaluate the critical flaw size for a through-wall axial crack:

$$l_{allow} = 1.58(R_m t)^{1/2} \left[ \left( \frac{\sigma_f}{\sigma_h} \right)^2 - 1 \right]^{1/2} \quad \text{Eq. 4-1}$$

where

$l_{allow}$  = allowable length of crack

$R_m$  = mean radius of canister

$t$  = thickness of shell

$\sigma_f$  = flow stress

$\sigma_h$  = hoop stress ( $p R_m / t$ )

- The equation in C-5330 is used to evaluate the critical flaw size for a through-wall circumferential crack. The equation is simplified since the load cases considered produce membrane stresses without bending.

$$2 \sin \left[ 0.5(\varphi - \theta_{allow}) \right] - \sin(\theta_{allow}) = \frac{\pi (\cancel{\sigma_b})}{2\sigma_f} \Rightarrow 0$$

$$\varphi = \pi \left( 1 - \frac{\sigma_m}{\sigma_f} \right) \quad \text{Eq. 4-2}$$

$$l_{allow} = (2R_m + t)\theta_{allow}$$

where

$\theta_{allow}$  = allowable circumferential half angle of crack

$\sigma_b$  = primary bending loads

$\sigma_m$  = primary membrane loads

- The equation in C-5420 is used to evaluate the allowable depth of an arbitrarily long axial flaw, and the equation may be simplified if a long flaw is assumed. In this instance, the equation reduces to setting the hoop stress in the remaining ligament equal to the flow stress:

$$\frac{a}{t_{allow}} = 1 - \frac{(SF_m)\sigma_h}{\sigma_f}$$

Because:

$$\frac{1 - a/t}{1 - \frac{a}{t} \left[ 1 + (1.61/4R_m t) l_{flaw}^2 \right]^{-1/2}} \Rightarrow \frac{1 - a/t}{1 - \frac{a}{t} [1 + (\gg 1)]^{-1/2}} \Rightarrow 1 - \frac{a}{t}$$

Eq. 4-3

where

$SF_m$  = structural factor, taken to be 1.0 since the flaws are hypothetical and are not being evaluated to remain in service

$a$  = crack depth

- Similar to the arbitrarily long part depth axial flaw, the equation in C-5322 for the allowable depth of an arbitrarily long circumferential (full circumference) flaw simplifies to setting the axial stress in the remaining ligament equal to the flow stress.

$$\sigma_m = \frac{\sigma_m^c}{(SF_m)} \Rightarrow \left(1 - \frac{a}{t_{allow}}\right) \sigma_f \tag{Eq. 4-4}$$

$$\text{because: } \sigma_m^c = \sigma_f \left[ 1 - \left(\frac{a}{t}\right) \left(\frac{\theta}{\pi}\right) - \frac{2}{\pi} \arcsin\left(\frac{a \sin \theta}{t/2}\right) \right] \Rightarrow \left(1 - \frac{a}{t}\right) \sigma_f$$

where

$\sigma_m^c$  = membrane stress for which a given size crack is the critical crack size

The results for each of the four load cases (normal and accident loads) defined in Table 4-1 are reported in Table 4-2 below. The critical crack size in the event that a canister is being moved after a crack has gone through-wall and relieved the internal pressure (handling loads only) is presented in Table 4-3. The results in these tables demonstrate that the canister designs are structurally very tolerant of the presence of flaws. Significant flaw lengths and depths are required to reach a critical flaw size.

**Table 4-2**  
**Results for Part Depth (PD) and Through-Wall (TW) Critical Flaw Size Calculations**

Load & Flaw Type		Units	NUHOMS 32PT	HI-STORM 24	NAC-UMS PWR	MAGNASTOR PWR
Normal	TW Axial	m	8.2	1.2	11.5	1.1
	TW Circ	m	4.0	3.3	4.0	3.3
	Max PD Axial	%t	98%	86%	98%	84%
	Max PD Circ	%t	98%	91%	98%	90%
Accident	TW Axial	m	1.2	0.6	2.6	0.4
	TW Circ	m	3.2	2.8	3.6	2.7
	Max PD Axial	%t	86%	73%	93%	64%
	Max PD Circ	%t	91%	84%	95%	80%

**Table 4-3  
Critical Flaw Size for Normal Handling Loads Only (No Internal Pressure)**

Flaw Type	Units	NUHOMS 32PT	HI-STORM 24	NAC-UMS PWR	MAGNASTOR PWR
Axial		No Rupture	No Rupture	No Rupture	No Rupture
TW Circ	m	4.2	4.1	4.2	4.3
Max PD Circ	%t	99%	98%	99%	98%

## 4.2 Tolerance for Loss of Helium Backfill

If a confinement boundary penetration were to occur, the helium backfill would be released and ambient air would begin to enter the canister by diffusion and thermal expansion/contraction of the gasses in the plenum. For significant helium backfill pressures such as those present in HI-STORM and MAGNASTOR canisters, a leak would lower the helium density, lowering the thermal performance and increasing the cladding temperature. For all designs, the ingress of oxygen would increase the peak cladding temperature due to the poorer thermal conductivity versus helium and would replace the inert atmosphere with an oxidizing one.

These scoping calculations model the transfer of gasses through the wall penetration using the equations in Section A.4.1, which are based on References [9] and [10]. This relation between pressure drop terms and the volumetric flow rate is developed in Reference [9] for leakage through SCC flaws from equations of laminar flow between parallel plates, a reasonable approximation for the small crack tip opening displacements calculated in Section 4.2.1. For the purposes of this calculation, it is assumed that the helium and air within the canister remain uniformly mixed. It is further assumed for simplicity that the canister internal temperature is a constant offset from ambient. Increases in the internal temperature as the canister depressurizes and air replaces helium are not modeled, and decreases in the internal temperature as the decay heat changes with storage time are not modeled. Such changes and changes in gas properties with temperature are shown to be second order effects on leak and ingress rates using sensitivity cases. Leakage calculations start at a characteristic initial pressure that is not adjusted for changes in internal temperature during storage.

### 4.2.1 Crack Opening Area

Crack opening area (COA) and crack opening displacement (COD) have a strong influence on the leak rate and air ingress calculations because they determine the idealized flow path geometry. The low primary stresses which occur during dry cask storage and branched nature of CISCC are expected to cause very small crack openings, and the elastic COA calculation performed in this assessment is likely to over-estimate the crack opening because it does not account for the branched and non-planar nature of SCC cracking. As such, the calculations are expected to provide lower bound time scales for helium leakage and air ingress.

The crack opening area is calculated using Reference [38], which provides an influence coefficient method solution to elastic crack opening area determined from the membrane and bending stresses. The crack opening displacement is calculated from the COA and crack length (2c) assuming an elliptical crack opening area, as shown in Figure 4-1. Assuming a rhomboid crack opening area would result in COD values larger by a factor of  $\pi/2$ , or 1.6. The crack

opening displacement model in Section D.7 of Reference [9] is found to produce similar results to the method used in this calculation.

The load cases evaluated are the same as those used in Section 4.1.1, except that the through-wall average weld residual stresses in Table 4-4 are conservatively applied as membrane loads for short flaw cases. As the crack grows longer, the residual strain in the center is relieved by the crack opening and the average opening stress due to WRS over the crack cross-section decreases. While Section 3.3.2 noted that through-wall penetration is expected to occur at short flaw lengths (e.g., about two times the wall thickness) longer flaw lengths are also considered as a sensitivity study in Table 4-5.

The crack opening results in Table 4-5 are simplified by presenting only the bounding results for each case. For load cases 1-6, only the highest WRS cases are considered as these will give the greatest crack opening: circumferential cracks subject to seam weld WRS and axial cracks subject to girth weld WRS. The COA and COD results in Table 4-5 are relatively insensitive to pressure and handling loads due to the large contribution of WRS (handling loads only add 2%), as shown by comparing the first and second cases in Table 4-5 against cases 7-10.

Including WRS, the calculated COD values for the most likely flaw sizes are on the order of 130  $\mu\text{m}$ . A brief literature review of failure analyses indicates that a typical COD for SCC flaws is on the order of 16-30  $\mu\text{m}$  [39]; the highly-branched nature typical of SCC produces much tighter flaws than results from an idealized planar through-wall crack assumed in the crack opening area analysis. Consequently, the results of this assessment provide conservatively large COAs that will bound the rate at which the backfill gas escapes the canister and is replaced by air. Because internal pressure has a small effect on COA, similar COA values are used for leakage and air ingress calculations, and the values are not varied as a function of the changing internal pressure. A COA of  $2.5 \times 10^{-6} \text{ m}^2$  is used for 25.4 mm long cracks based on cases 1, 7, and 8, and a COA of  $1.0 \times 10^{-5} \text{ m}^2$  is used for 100 mm long cracks based on cases 3, 9, and 10.

**Table 4-4**  
**Weld Residual Stress Values [1] Used in the Crack Opening Displacement Analysis**

WRS Orientation	Average TW WRS (MPa)	
	Girth Weld	Seam Weld
Hoop Stress	434.42	0.12
Axial Stress	0.77	445.19

**Table 4-5**  
**Crack Opening Area Results for Larger of Seam and Girth Weld Cases for Bounding Canister Designs**

Case	Case Description	Design Internal Pressure [MPa (psig)]	Shell Thickness (mm)	Crack Length		Crack Opening Area (m <sup>2</sup> )		Crack Opening Displacement <sup>(4)</sup> (mm)	
				(Multiples of Shell Thick.)	(mm)	Axial	Circumferential	Axial	Circumferential
1	Bounding Normal Loads (Low)	0.10 (15)	15.9	1.6	25.4	2.36E-06	2.37E-06	0.12	0.12
2	Bounding Accident Loads (High)	1.72 (250)	12.7	2.0	25.4	3.01E-06	2.71E-06	0.15	0.14
3	Low Loads, Large Flaw Length <sup>(1)</sup>	0.10 (15)	15.9	6.3	100	1.16E-05	1.05E-05	0.15	0.13
4	High Loads, Large Flaw Length <sup>(1)</sup>	1.72 (250)	12.7	7.9	100	2.37E-05	1.64E-05	0.30	0.21
5	Low Loads, Very Large Flaw Length <sup>(2)</sup>	0.10 (15)	15.9	31	500	4.99E-05	2.89E-05	0.13	0.07
6	High Loads, Very Large Flaw Length <sup>(2)</sup>	1.72 (250)	12.7	39	500	1.17E-03	2.96E-04	3.0	0.75
7	WRS Only (Girth Weld), All Canister Designs <sup>(3)</sup>	0	12.7 – 15.9	1.6 – 2.0	25.4	~2.3E-06	~0	~0.12	~0
8	WRS Only (Seam Weld), All Canister Designs <sup>(3)</sup>	0	12.7 – 15.9	1.6 – 2.0	25.4	~0	~2.3E-06	~0	~0.12
9	¼ WRS Only (Girth Weld), All Canister Designs <sup>(3)</sup>	0	12.7 – 15.9	6.3 – 7.9	100	~1.1E-05	~0	~0.14	~0
10	¼ WRS Only (Seam Weld), All Canister Designs <sup>(3)</sup>	0	12.7 – 15.9	6.3 – 7.9	100	~0	~9.9E-06	~0	~0.13

**Notes:**

1. The WRS applied to this case is a one-fourth of the nominal values in Table 4-4.
  2. No weld residual stress is applied to this case due to the large flaw size.
  3. This case applies to flaws of this size for each of the four canister geometries evaluated in Table 4-1.
- As mentioned above, COD is determined from the COA and crack length assuming a perfectly elliptical crack opening area

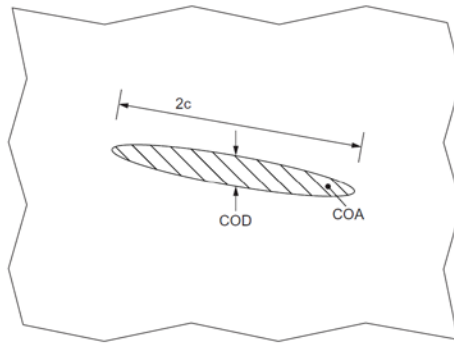


**Figure 4-1**  
**Diagram of Crack Opening for Idealized Through-Wall Flow**

### **4.2.2 Helium Leakage**

Canister depressurization is calculated to occur rapidly relative to the timescales expected for processes such as air ingress or crack growth. The main inputs and key results for the leakage analysis are presented in Table 4-6. For simplicity, inputs are not adjusted to account for changes in decay heat, and internal temperature is not dependent on the canister internal gas composition. Results are presented in terms of volumetric flowrate at internal conditions and time from start of leakage until a gauge pressure of 5% of atmospheric pressure (absolute pressure of 106 kPa, 15.4 psia) is reached.

Among the different cases considered which explore the canister geometry, the primary differences are the initial backfill pressure (compare cases 1 and 4 to cases 2 and 3), the free volume within the canister (compare case 1 to case 4 and case 2 to case 3), and the wall thickness (compare case 2 to case 3). While canister geometry variables such as wall thickness and internal free volume are not as important, the internal pressure can affect the leak rate and time by a factor of two. These factors remain second order effects when compared with the dependence of leakage rate on COD and crack opening area (comparing cases 1 and 2 to cases 5 and 6 and cases 7 and 8). While the backfill gas pressure and temperature are dependent on the instantaneous decay power of a canister, the analysis assumes a characteristic value for the pressure and temperature. Based on the results of the internal pressure cases, this assumption is not expected to significantly affect the results.

For cracks transverse to the weld that are opened by WRS and normal loads (see Section 4.2.1), the time for the internal pressure to reach a gauge pressure of 5% of atmospheric pressure ranges from about an hour for relatively large flaws with lengths approaching 100 mm (cases 5 and 6) to a few hours for tight flaws with lengths closer to twice the shell thickness (cases 1 and 2). For crack opening displacements consistent with the typical SCC flaw openings comparable to those in literature (on the order of 16-30  $\mu\text{m}$ ), the time for the canister to reach near ambient pressure is a few weeks (cases 7 and 8).

**Table 4-6  
Leak Rate Inputs and Results**

Inputs <sup>(1)</sup>							Results	
Case	Shell Thickness (mm)	Internal Free Volume (m <sup>3</sup> )	Initial Internal Pressure [MPa(psig)]	Crack Length (mm)	COA (m <sup>2</sup> )	Elliptical COD (μm)	Maximum Calculated Leak Rate (cm <sup>3</sup> /s)	Time to 105% Atmospheric Pressure (days)
1	12.7	6.76	0.69(100)	25	2.5E-06	127	943	0.39
2	12.7	3.77	0.10(15)	25	2.5E-06	127	484	0.14
3	15.9	5.74	0.10(15)	25	2.5E-06	127	431	0.24
4	12.7	6.56	0.76(110)	25	2.5E-06	127	960	0.38
5	12.7	6.76	0.69(100)	100	1.0E-05	127	3774	0.097
6	12.7	3.77	0.10(15)	100	1.0E-05	127	1936	0.034
7	12.7	6.76	0.69(100)	25	4.0E-07	20	28.7	52
8	12.7	3.77	0.10(15)	25	4.0E-07	20	4.44	24

**Notes:**

1. As noted in Section 2.2.2, the internal temperature for all cases is 150°C, and the external conditions are 25°C and 101 kPa.

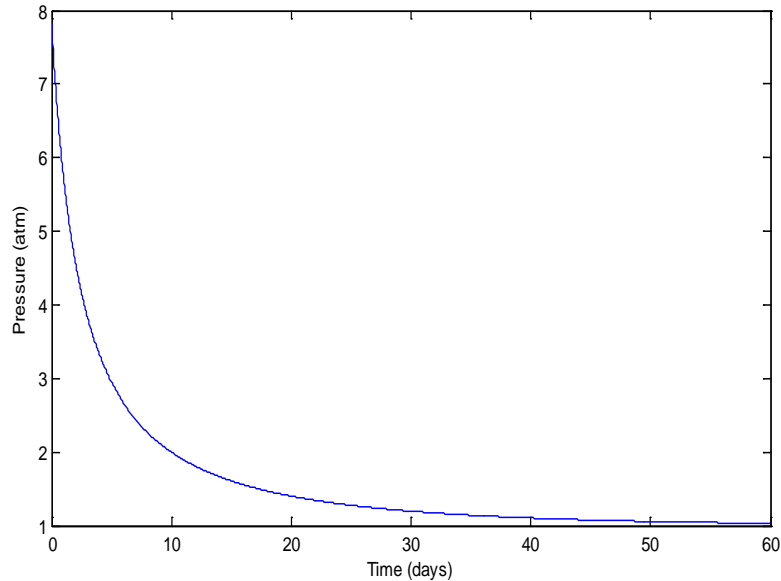


**Figure 4-2**  
**Results of Leakage Analysis for Case 7 of Table 4-6**

### 4.2.3 Air Ingress

The constrained volume of the canister provides the potential for pressure differences between the atmosphere and canister interior based on diurnal and seasonal ambient pressure and temperature variations. These variations can cause a breathing or pumping effect that replaces the helium backfill with air at a rate faster than diffusion. The air ingress calculation is a function primarily of the crack size and the diurnal temperature variation experienced by the canister.

An evaluation of the effects of air ingress on the fuel assemblies within the canister is performed in the FMEA report [1]. If there are fuel rods in the canister that are breached and have elevated fuel temperatures in the vicinity of the breach, then the presence of an oxidizing atmosphere could cause fuel pellet swelling that could degrade the cladding of those fuel rods. These conditions are not expected to be applicable to the majority of the fuel inventory. The majority of the fuel inventory is expected to be intact, and fuel temperatures after sufficient storage time are low enough to preclude swelling.

The air ingress calculation in this section starts with the canister internal pressure at equilibrium with the external conditions and maintains the canister internal temperature at the same offset from ambient as is used in the leakage calculation (offset of 125°C based on internal 150°C and external 25°C). The reported results are the time from this equilibrium until the target molar air fraction (50% or 90%) is reached. This calculation is decoupled from the results of the leakage calculation in Section 4.2.2.

Two types of temperature variation are considered in this evaluation. For the first part of this analysis, a sinusoidal temperature variation with an amplitude of 15°C is assumed, and the results are presented in Table 4-7. A second evaluation is performed using the full set of measured ambient temperature and pressure data from monitoring stations with results in Table 4-8. Comparing the results of Table 4-7 and Table 4-8 indicates that air ingress rates calculated

using the assumed daily temperature variation of 15°C bound the ingress rates calculated using actual site data.

According to the hourly data from the two monitoring stations, the ambient pressure remained within about 2% of the annual average pressure. The amplitude of the seasonal temperature variation was about 8°C at Camp Pendleton, CA and 15°C at Patuxent, MD. The amplitude of the diurnal temperature variation was about 10°C at both sites evaluated. At the beginning of the annual dataset used, there was greater diurnal climate variation at Camp Pendleton than Patuxent, leading to more rapid air ingress through larger cracks with less flow restriction (case 1 vs. 7 of Table 4-8). Seasonal temperature variations at Patuxent are larger, so air ingress through a smaller crack is more rapid in case 5 (Patuxent) than case 8 (Camp Pendleton).

Ingress through a large crack is limited by fluctuations in atmospheric conditions rather than the leak rate (cases 5 and 6 of Table 4-7), leading to similar replacement rates for different canister internal volumes. For small crack opening areas, the rate of air ingress is limited by the volumetric flow rate through the crack (cases 7 and 8 of Table 4-7), so the internal volume has a notable effect. The results of the sensitivity cases for internal temperature (cases 9 and 10 of Table 4-8) indicate that assuming a lower gas temperature is conservative with regards to the time taken for air ingress and that assuming the internal temperature remains constant as air enters is similarly conservative.

The air ingress phase is expected to take orders of magnitude longer to occur than the release of pressure. For instance, the crack size which took a few weeks to reach a gauge pressure of 5% of atmospheric pressure takes years to reach even a molar fraction of 50% air. These time frames are consistent with the observed air ingress at a leaking bolted cask reported in Reference [40], which took seventeen months to go from about 33% to 75% air.

**Table 4-7**  
**Ingress Cases for Large Sinusoidal Daily Temperature Variation**

Inputs						Results	
Case	Shell Thickness (mm)	Internal Free Volume (m <sup>3</sup> )	Daily Variation of T (°C)	Crack Length (mm)	COA (m <sup>2</sup> )	Time to 50% Air (days)	Time to 90% Air (days)
1	12.7	6.76	30	25	2.5E-06	10.5	34.4
2	12.7	3.77	30	25	2.5E-06	9.7	32.7
3	15.9	5.74	30	25	2.5E-06	10.5	34.5
4	12.7	6.56	30	25	2.5E-06	10.5	34.4
5	12.7	6.76	30	100	1.0E-05	9.6	32.5
6	12.7	3.77	30	100	1.0E-05	9.6	32.5
7	12.7	6.76	30	25	4.0E-07	780	2573
8	12.7	3.77	30	25	4.0E-07	435	1434

**Table 4-8**  
**Ingress Cases Using Measured Hourly Atmospheric Pressure and Temperature Data**

Inputs						Results	
Case	Shell Thickness (mm)	Internal Free Volume (m <sup>3</sup> )	Atmospheric Data Source	Crack Length (mm)	COA (m <sup>2</sup> )	Time to 50% Air (days)	Time to 90% Air (days)
1	12.7	6.76	Camp Pendleton	25	2.5E-06	28.1	74.5
2	12.7	3.77	Camp Pendleton	25	2.5E-06	25.1	67.1
3	15.9	5.74	Camp Pendleton	25	2.5E-06	28.2	75.0
4	12.7	6.56	Camp Pendleton	25	2.5E-06	28.0	74.2
5	12.7	6.76	Camp Pendleton	25	4.0E-07	1629	5581
6	12.7	3.77	Camp Pendleton	25	4.0E-07	926	3179
7	12.7	6.76	Patuxent, MD	25	2.5E-06	32.6	90.8
8	12.7	6.76	Patuxent, MD	25	4.0E-07	1417	4620
9 <sup>(1)</sup>	12.7	6.76	Camp Pendleton	25	4.0E-07	1532	4956
10 <sup>(2)</sup>	12.7	6.76	Camp Pendleton	25	4.0E-07	1880	6100

**Notes:**

1. This sensitivity study on case 5 assumed a 75°C offset between the internal gas temperature and external ambient (an offset of 125°C is used in case 5).
2. This sensitivity study on case 5 assumed a 175°C offset between the internal gas temperature and external ambient (an offset of 125°C is used in case 5).

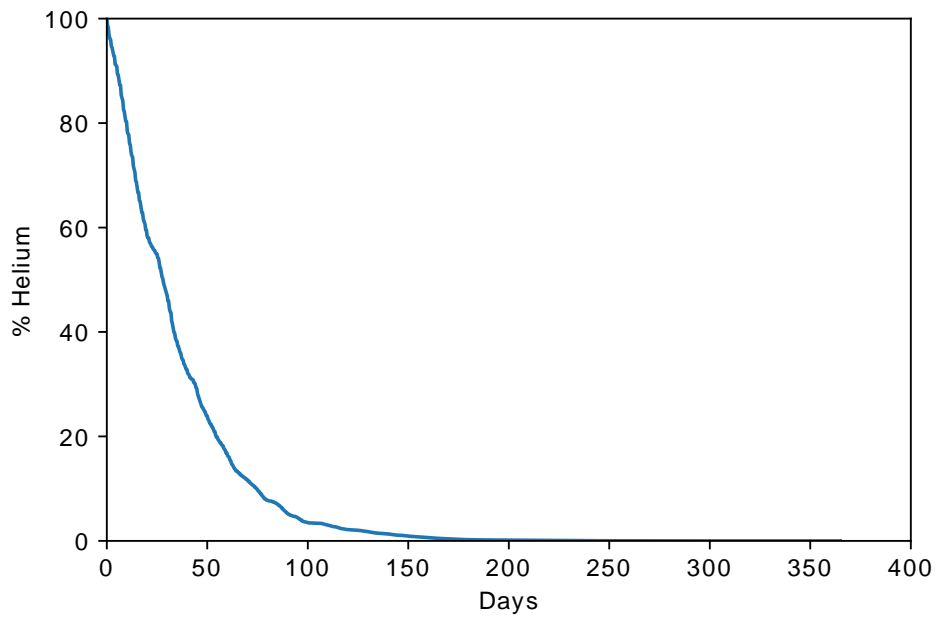


**Figure 4-3**  
**Results of Air Ingress Analysis for Case 1 of Table 4-8**



# 5

## CONCLUSIONS

This technical update documents: 1) a deterministic calculation of CISCC flaw growth in stainless steel canisters, and 2) the structural tolerance of the canisters to flaws. These calculations provide initial estimates of the resistance of DCSS stainless steel canisters to chloride-induced degradation. The timeframes calculated in this section do not consider the time required to develop conditions leading to crack initiation, which are expected to be substantial.

### 5.1 Flaw Propagation Calculation

Flaw propagation is only expected to occur at positions on the canister which meet all of the following conditions: (1) a substantial accumulation of chlorides is present, and (2) the surface temperature is cool enough to experience deliquescence for a meaningful fraction of the year (typically, less than 30°C above ambient), and (3) sufficient through-wall tensile stress is present; i.e., located within about four wall thicknesses of a weld.

The primary inputs to the crack growth rate model are the site climate and the surface temperature at the location of interest on the canister; there is no modeled variation in flaw growth at similar temperature for different flaw orientations or on different canister types. As the flaw penetrates beyond a threshold depth, the growth rate is modeled as having a reduced crack growth rate based on multiple experimental observations of an apparent rate limiting effect. As the surface temperatures decay with time, the increasing duty factor for the fraction of time subject to deliquescence is offset by reduced thermal acceleration of the CISCC process. This results in a peak CGR value generally predicted at a canister surface temperature that is 15-20°C above ambient. For sites with an average annual AH around 10 g/m<sup>3</sup>, the predicted growth rate is about two times less than for those with an average annual AH near 20 g/m<sup>3</sup>. The crack growth calculations are performed using a large number of conservatisms both in modeling approach and statistical treatment of data; it may be appropriate to reduce these conservatisms if additional data becomes available.

### 5.2 Flaw Tolerance Evaluation

The critical flaw sizes calculated for the load cases evaluated are large and demonstrate the structural robustness of the canister. It is noted that the interior pressure serves as the primary source of stress for canisters on the pad, so the critical flaw size in the event of a retrieval handling load would increase significantly if a smaller flaw were to grow through-wall and relieve the internal pressure.

In the event of a through wall crack, the time required for any depressurization of the helium backfill is short relative to the timescale of the other processes evaluated, and the timescale for helium replacement with air is heavily dependent on the through-wall flaw geometry. For very tight cracks and small crack opening areas typical of SCC cracks, the time required for the canister to have an appreciable mole fraction of air can be on the order of years. The timescale of air ingress indicates that if monitoring for loss of helium occurred, action could be taken before substantial concentrations of air entered the canister.

### **5.3 Modeling Considerations**

The modeling performed in this assessment focused on using the available data to predict the growth rate of CISCC in heated stainless steel exposed to atmospheric chloride in a sheltered environment and the effect of such flaws on canister behavior. Additional testing may be appropriate to verify certain aspects of the approach to flaw growth modeling and determine the dependence of growth on additional environmental factors. The values of crack growth parameters used in this assessment are developed from the available atmospheric testing data; if and when additional data becomes available, the parameters should be revisited.

# 6

## REFERENCES

1. *Failure Modes and Effects Analysis (FMEA) of Welded Stainless Steel Canisters for Dry Cask Storage Systems*. EPRI, Palo Alto, CA: 2013. 3002000815.
2. *Literature Review of Environmental Conditions and Chloride Induced Degradation Relevant to Stainless Steel Canisters in Dry Cask Storage Systems*. EPRI, Palo Alto, CA: 2014. 3002002528.
3. R. Parrott and H. Pitts, *Chloride stress corrosion cracking in austenitic stainless steel – recommendations for assessing risk, structural integrity and NDE based on practical cases and a review of literature*, Health & Safety Laboratory, ES/MM/09/48, 2010.
4. R. Hosler, “Screening Criteria for ID and OD-Initiated SCC of Pressure Boundary Stainless Steel Components (Phase 1 of I&E Guideline Development),” AREVA document 51-9142337-000, October 18, 2010.
5. A. Kosaki, “Evaluation Method of Corrosion Lifetime of Conventional Stainless Steel Canister under Oceanic Air Environment,” *Nuclear Engineering and Design*, Vol. 238, No. 5, p. 1233–1240. 2008.
6. K. Shirai, J. Tani, and T Saegusa. *Study on Interim Storage of Spent Nuclear Fuel by Concrete Cask for Practical Use -Feasibility Study on Prevention of Chloride Induced Stress Corrosion Cracking for Type 304L Stainless Steel Canister*, CRIEPI N10035, 2011. (In Japanese)
7. NOAA National Climatic Data Center, *Climate Data Online*. <http://www.ncdc.noaa.gov/cdo-web/>
8. X. He, T.S. Mintz, R. Pabalan, L. Miller, and G. Oberson, *Assessment of Stress Corrosion Cracking Susceptibility for Austenitic Stainless Steels Exposed to Atmospheric Chloride and Non-Chloride Salts*, Southwest Research Institute, NUREG/CR-7170, February 2014.
9. *Effects of Marine Environments on Stress Corrosion Cracking of Austenitic Stainless Steels*, EPRI, Palo Alto, CA: 2005. 1011820.
10. *SQUIRT: Seepage Quantification of Upsets In Reactor Tubes User's Manual*, Windows Version 1.1, March 24, 2003.
11. J.M. Cuta, S.R. Suffield, J.A. Fort, H.E. Adkins, *Thermal Performance Sensitivity Studies In Support Of Material Modeling For Extended Storage Of Used Nuclear Fuel*, PNNL-22646, 2013.
12. A.J. Mansure and S.V. Petney, *Determination of Equivalent Thermal Loadings as a Function of Waste Age and Burnup. Yucca Mountain Site Characterization Project*. Sandia National Laboratories, SAND87-2909, April 1991.
13. S. Suffield, et al., “Thermal Modeling of NUHOMS HSM-15 and HSM-1 Storage Modules at Calvert Cliffs Nuclear Power Station ISFSI,” PNNL-21788, Pacific Northwest Research Laboratory, October 2012.

14. G.J. Banken, "Thermal Analysis of NUHOMS Advanced Horizontal Storage Module Using CFD Method," Transnuclear, Calculation SCE-20.0410NP Rev. 2, 2004. (ADAMS Accession No. ML042220037)
15. MAGNASTOR (Modular Advanced Generation Nuclear All-purpose STORAge) Safety Analysis Report, NAC International, Rev. 2, 2008. (Available with NRC Accession Nos. ML083170473, ML081710155)
16. J.M. Cuta, H.E. Adkins, *Preliminary Thermal Modeling of HI-STORM 100S-218 Version B Storage Modules at Hope Creek Nuclear Power Station ISFSI*, PNNL-22552, Pacific Northwest Research Laboratory, August 2013.
17. *Performance Testing and Analyses of the VSC-17 Ventilated Concrete Cask*, EPRI, Palo Alto, CA: 1992. TR-100305.
18. *Materials Reliability Program: Assessment of the Current Status and Completeness of Work on Inner and Outer Diameter Stress Corrosion Cracking of Austenitic Stainless Steels in PWR Plants (MRP-352)*. EPRI, Palo Alto, CA: 2013. 3002000135.
19. T. Prosek, et. al, "Low temperature stress corrosion cracking of austenitic and duplex stainless steels under chloride deposits," *Corrosion*, 2014.
20. J. I. Tani, "Initiation and Propagation of Stress Corrosion Cracking of Stainless Steel Canister for Concrete Cask Storage of Spent Nuclear Fuel," *Corrosion*, Vol. 65, No. 3, p. 187-194, © NACE International 2009.
21. D.D. Macdonald, "Fate of the Coupling Current in Stress Corrosion Cracking-Mechanistic and Corrosion Control Implications," *CORROSION*, Paper No. 04570, 2004.
22. A. Cook, et al., "Atmospheric-Induced Stress Corrosion Cracking Of Austenitic Stainless Steels Under Limited Chloride Supply," *18th International Corrosion Congress*, 2011.
23. A. Cook, et al., "Under-Deposit Chloride-Induced Stress Corrosion Cracking in Austenitic Stainless Steels: Aspects Associated with Deposit Type, Size and Composition" *ECS Transactions*, Vol. 58 No. 29 pp. 25-39, 2014.
24. O. E. Albores-Silva, E. A. Charles, and C. Padovani, "Effect of Chloride Deposition on Stress Corrosion Cracking of 316L Stainless Steel Used for Intermediate Level Radioactive Waste Containers," *Corrosion Engineering*, Vol. 46, No. 2, 2011.
25. L. Caseres and T. S. Mintz, NUREG/CR-7030, "Atmospheric Stress Corrosion Cracking Susceptibility of Welded and Unwelded 304, 304L, and 316L Austenitic Stainless Steels Commonly Used for Dry Cask Storage Containers Exposed to Marine Environments," U.S. Nuclear Regulatory Commission, Washington DC, 2010.
26. P. Chen, T. Shinohara, S. Tsujikawa, "Applicability of the Competition Concept in Determining the Stress Corrosion Cracking Behavior of Austenitic Stainless Steels in Chloride Solutions," *Zairyo-to-Kankyo*, Vol. 46, No. 5, p. 313-320, 1997.
27. R.G. Kelly, et al., "Considerations of the Role of the Cathodic Region in Localized Corrosion" Yucca Mountain Project, U.S. Department of Energy, March 17, 2006. (Available at <https://www.osti.gov/servlets/purl/893928-5RrmfH/>)
28. A.S. Agarwal, U. Landau, and J.H. Payer, "Modeling Particulates Effects on the Cathode Current Capacity in Crevice Corrosion," *Journal of the Electrochemical Society*, Vol. 155, No. 5, 2008.

29. S. Wang, "Conditions for stress corrosion cracking to occur from crevice corrosion sites and related electrochemical features," *Materials and Corrosion*, Vol. 55, No. 12, 2004.
30. M. Wataru, "Japanese Current Status of Dry Storage and Aging Management Methodology and CRIEPI's Researches," Presentation at *Extended Storage Collaboration Program (ESCP)*, December 5, 2013.
31. Y. Toshima, et al., "Long-Term Exposure Test for External Stress Corrosion Cracking on Austenitic Stainless Steels in Coastal Areas," *CORROSION 2000*, Paper No. 00456, © NACE International 2000.
32. Letter from J.A. Stall to U.S. NRC, "ECCS Suction Header Leaks Result in Both ECCS Trains Inoperable and TS 3.0.3 Entry," LER 1999-003-00, May 6, 1999.
33. R. Hosler and J. Hall, "Outside Diameter Initiated Stress Corrosion Cracking Revised Final White Paper," PWROG document PA-MS-C-0474, October 13, 2010. (Available with NRC Accession No. ML110400241)
34. *Holtec International Final Safety Analysis Report for the HI-STORM 100 Cask System*, Holtec International, Rev. 9, 2010. (Available with NRC Accession No. ML101400161)
35. NAC-UMS Universal MPC System Final Safety Analysis Report (FSAR), Revision 3, NAC International, 2004. (Available with NRC Accession Nos. ML051290397, ML041040369, ML051290403, ML041040397)
36. MAGNASTOR (Modular Advanced Generation Nuclear All-purpose STORage) Safety Analysis Report, NAC International, Rev. 2, 2008. (Available with NRC Accession Nos. ML083170473, ML081710155)
37. *Final Safety Analysis Report for the Standardized NUHOMS Horizontal Modular Storage System for Irradiated Nuclear Fuel*, Transnuclear Inc., NUH-003.0103, Rev. 8, 2004. (Available with NRC Accession No. ML042110421)
38. T. L. Anderson, et al., "Stress Intensity and Crack Growth Opening Area Solutions for Through-Wall Cracks in Cylinders and Spheres," *Welding Research Council Bulletin* 478, January 2003.
39. R. M. Meyer, et al., "Evaluating Conventional NDE Methods for Crack Detection in Metal Canisters," Presentation at *Extended Storage Collaboration Program (ESCP)*, December 4, 2013.
40. "CPP-2707 Cask Assessment During 2008," Idaho Nuclear Technology and Engineering Center, EDF-9069 Rev. 0, 2009.
41. O.O. Parish and T.W. Putnam, Equations for the Determination of Humidity from Dewpoint and Psychrometric Data, NASA Technical Note, TN D-8401, January 1977.
42. S. Carroll, L. Craig, and T. Wolery, "Deliquescence of NaCl–NaNO<sub>3</sub>, KNO<sub>3</sub>–NaNO<sub>3</sub>, and NaCl–KNO<sub>3</sub> Salt Mixtures from 90 to 120°C," *Geochemical Transactions*, Vol. 6, No. 2, p. 19-30, June 2005.
43. G. Oberson, D. Dunn, T. Mintz, et al., "US NRC-Sponsored Research on Stress Corrosion Cracking Susceptibility of Dry Storage Canister Materials in Marine Environments," *WM2013 Conference*, 2013. (Available with NRC Accession No. ML13029A490)

44. S. Shoji and N. Ohnaka, "Effects of Relative Humidity and Chloride Type on Stainless-Steel Room-Temperature Atmospheric Corrosion Cracking," *Corrosion Engineering*, Vol. 38, p. 111-119, 1989.
45. L. Greenspan, "Humidity Fixed Points of Binary Saturated Aqueous Solutions," *Journal of Research of the National Bureau of Standards*, Vol. 81A, No. 1, 1977.
46. C. Bryan, *Analysis of Dust Deliquescence for FEP Screening*, Bechtel SAIC Co., ANL-EBS-MD-000074, Rev. 01, 2005.
47. *Materials Reliability Program: Technical Bases for the Chemical Mitigation of Primary Water Stress Corrosion Cracking in Pressurized Water Reactors (MRP-263 NP)*. EPRI, Palo Alto, CA: 2012. 1025669.
48. ASME Boiler and Pressure Vessel Code, Section XI, Division 1, Nonmandatory Appendix C, Evaluation of Flaws in Piping, 2013 Edition.
49. K. Shirai, et al., "Research on Spent Fuel Storage and Transportation in CRIEPI (Part 2 Concrete Cask Storage)," *16th Pacific Basin Nuclear Conference (16PBNC)* held in Aomori, Japan, Paper No. P16P1215, October 13-18, 2008.
50. M. Yajima and M. Arii, "Chloride Stress Corrosion Cracking of AISI 304 Stainless Steel in Air," *Materials Performance*, Vol. 19, No. 10, p. 17-19, © NACE International 1980.
51. H. Hayashibara, M. Mayuzumi, Y. Mizutani and J. Tani, "Effects of Temperature and Humidity on Atmospheric Stress Corrosion Cracking of 304 Stainless Steel," *NACE Corrosion*, Paper No. 08492, © NACE International 2008.
52. H. Hayashibara, M. Mayuzumi, Y. Mizutani and J. Tani, "Effects of Temperature and Humidity on Atmospheric Stress Corrosion Cracking of 304 Stainless Steel," *NACE Corrosion*, Paper No. 08492, Figure 10 on p. 8, © NACE International 2008.
53. N. D. Fairweather, N. Platts, and D. R. Tice, "Stress-Corrosion Crack Initiation of Type 304 Stainless Steel In Atmospheric Environments Containing Chloride: Influence Of Surface Condition, Relative Humidity, Temperature and Thermal Sensitization," *NACE Corrosion 2008*, New Orleans, © NACE International 2008.
54. K. Shirai, et al., "SCC Evaluation Test of a Multi-Purpose Canister," *International Conference on High Level Radioactive Waste Management*, Albuquerque, p. 824-831; Paper No. 3333, 2011.
55. O. E. Albores-Silva, E. A. Charles, and C. Padovani, "Effect of Chloride Deposition on Stress Corrosion Cracking of 316L Stainless Steel Used for Intermediate Level Radioactive Waste Containers," *Corrosion Engineering*, Vol. 46, No. 2, 2011.
56. P. Roberge, *Handbook of Corrosion Engineering*, McGraw-Hill: New York, NY, 2000.
57. J.C. Newman and I.S. Raju, "Analyses of Surface Cracks in Finite Plates Under Tension or Bending Loads," NASA Technical Paper 1578, 1979.
58. D. Montgomery and G. Runger, *Applied Statistics and Probability for Engineers*, John Wiley & Sons, Inc., New York, NY 1994.
59. J.P. Holman, *Heat Transfer*, 10<sup>th</sup> Ed., McGraw Hill: New York, NY, 2010.

# A

## MODEL DETAILS AND INPUTS

This appendix describes the models which are used to simulate the propagation of flaws through the canister wall and the potential consequences of a through-wall crack. Whereas the main body of the report focuses on the overarching approach to modeling and the results of the analyses, this appendix is used to provide reader with the modeling details and equations that underlie the conclusions of the report.

### A.1 Humidity, Climate, and Deliquescence

This section describes the retrieval and application of climate data and describes the treatment of the deliquescent relative humidity of sea salt. Conversions among dew point, AH, and RH as a function of temperature are performed as described in a NASA Technical Note [41]. The model yields an error of less than 1% against meteorological tables from -50°C to 100°C.

#### A.1.1 Deliquescence Model

Deliquescence of a hygroscopic material is defined as the point where a material absorbs enough water to enter solution. In DRH testing performed with conductivity measurements and in simulations, the DRH of sea salt is similar to or slightly lower than the DRH of MgCl<sub>2</sub> (about 33% RH at room temperature). The DRH of sea salt is observed to be lower than both NaCl and MgCl<sub>2</sub> because the thermodynamic equilibrium of a mixed brine results in saturation concentrations of both constituents, reducing the water activity and the vapor pressure [42]. For a mixture of species with different DRH values, the deliquescence point of the mixture is generally between that of the individual species; for a mixture of species with similar DRH values, the mutual deliquescence point is generally lower than that of the individual species [42]. The minor presence of calcium in sea salt does not lower the DRH to levels seen for CaCl<sub>2</sub>. At humidities just below the DRH, hygroscopic absorption forms a wetted layer around salt crystals which may be sufficient to initiate localized corrosion, but the small and isolated nature of these surface cathodes would be expected to preclude growth of a macroscopic flaw.

In order to capture these effects, the DRH model is based on the lower bound for the results of impedance testing used to measure the DRH and ERH [8]. In this way, the low DRH used in this work conservatively permits crack growth in this humidity regime and at humidities where hysteresis would lead to a dry salt. Choosing such a conservative DRH also implicitly accounts for any retention of absorbed water at humidities below the deliquescent RH by capillary forces.

Atmospheric CISCC initiation with sea salt is not observed below about 25% to 35% RH (140°F-120°F, or 60°C-50°C, assuming an AH of 30 g/m<sup>3</sup>) ([43] and [44]). As seen by the plotted data points in Figure A-1, DRH and ERH data for sea salt are generally consistent with this band.

The deliquescence relative humidity of sea salt as a function of temperature is calculated as a constant offset from the DRH curve for MgCl<sub>2</sub> from Reference [45]. The MgCl<sub>2</sub> curve has a range of applicability from 0.0°C to 99.4°C and uses absolute temperature,  $T$  (K). In this work,

an offset ( $\Delta_{offset}$ ) of 7% RH was chosen to obtain DRH values for sea salt which lie at the lower ERH values obtained in recent testing [8] over the range of relevant conditions.

$$DRH(T) = \left[ 33.67 - 7.974 \times 10^{-3} (T - 273.15) - 1.090 \times 10^{-3} (T - 273.15)^2 \right] / (100 - \Delta_{offset}) \quad \text{Eq. A-1}$$

The estimated deliquescent relative humidity for sea salt,  $DRH$ , using Equation A-1 and an offset of 7% RH, is plotted in Figure A-1 against measured deliquescence data and curves of constant AH generated by the relations in Reference [41]. Figure A-1 shows that the model—using Equation A-1 and an offset of 7% RH—conservatively falls at or below the lowest measured DRH/ERH values.

The presence of non-deliquescent species (e.g., pollen) would tend to increase the volumetric resistivity of any deliquescent solution [27], decreasing its effectiveness in supporting active corrosion. While non-deliquescent species do not directly affect the DRH of the mixture, the effective ERH might be lowered if such a non-deliquescent deposit exhibited small pores with a strong capillary action. However, such capillary action might also sequester the deliquescent brine away from the surface [46]. The DRH offset discussed above introduces sufficient conservatism that explicit consideration of the potential detrimental effects of non-deliquescent deposit constituents is not necessary.

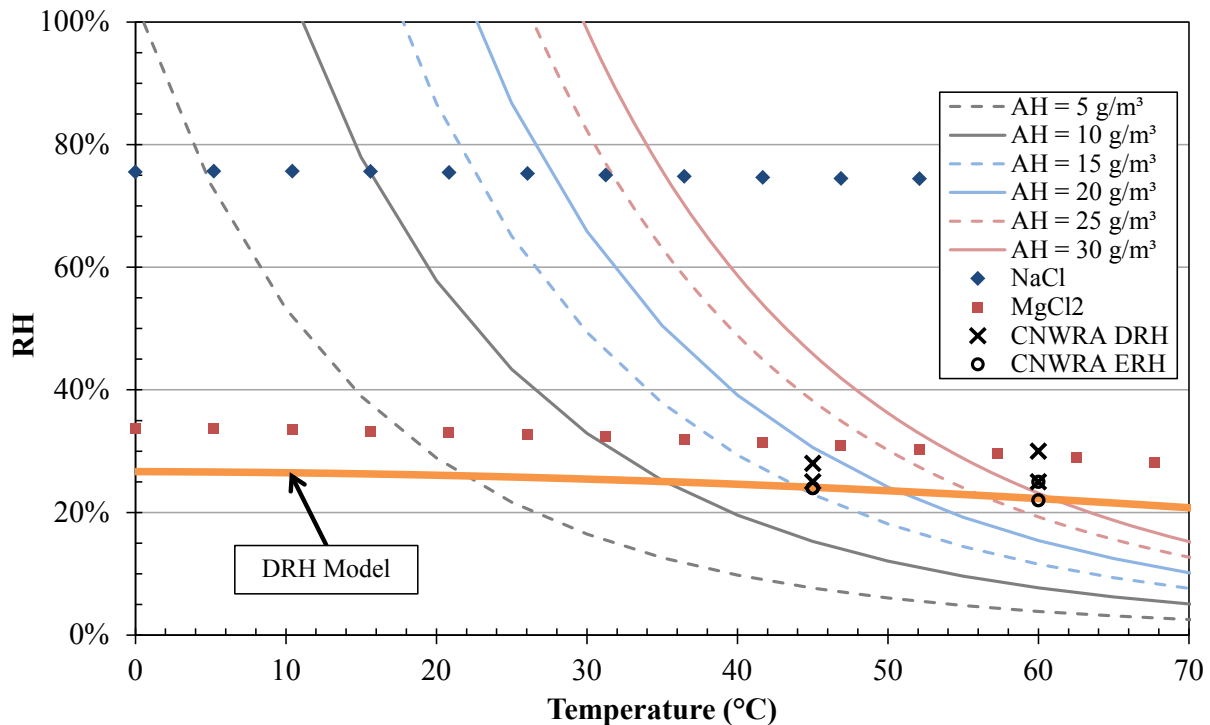


**Figure A-1**  
**DRH Model, CNWRA Sea Salt DRH Data [8], and Standard DRH Curves for Various Salts [45]**  
**Plotted for Temperature and RH on Curves of Constant AH**

### **A.1.2 Process to Obtain Hourly Local Climate Data**

The hourly climate data over a typical year for a large number of U.S. and international sites is available from Reference [7] and can be obtained as described below.

- Visit the NOAA National Climatic Data Center [7]
  - Click on “Mapping Tool” > “All Maps” tab > “Global Hourly Surface Data”
  - Alternatively, visit:  
<http://gis.ncdc.noaa.gov/map/viewer/#app=cdo&cfg=cdo&theme=hourly>
- In the “Layers” window, ensure that “Hourly Global” is visible (the box is checked)
- Pan and zoom to the location of interest, or click on the red flag in the “Select Tools” window to show a given location (e.g., a U.S. zip code)
- In the “Select Tools” window, choose a select tool to select relevant sites
- In the “Results” window, select the desired site with appropriate start and end dates, then “Get Selected Data”
- From the “Data Access Options” window, choose "Advanced", then “Access Data”
- Choose “Air Temperature Observation” and “Air Temperature Observation Dewpoint” then click continue
  - The following parameters are not involved in calculations for this assessment, but may be otherwise desired: “Relative Humidity Calculation,” “Wind Direction,” and “Wind Observation” (values from “Relative Humidity Calculation” are essentially identical to those calculated from the dew point using Reference [41], which is the preferred method)
- Select at least one year’s worth of data, then follow the onscreen instructions to submit the request for data
- Import the data and filter to eliminate null values

The hourly dew point and temperature data for an entire year data for a variety of sites has been analyzed to determine the fraction of time for which the AH at a given site is above a given value. These results are plotted in Figure A-2 and are used in the calculation of  $f_H$ , described in Section A.2.2.3.

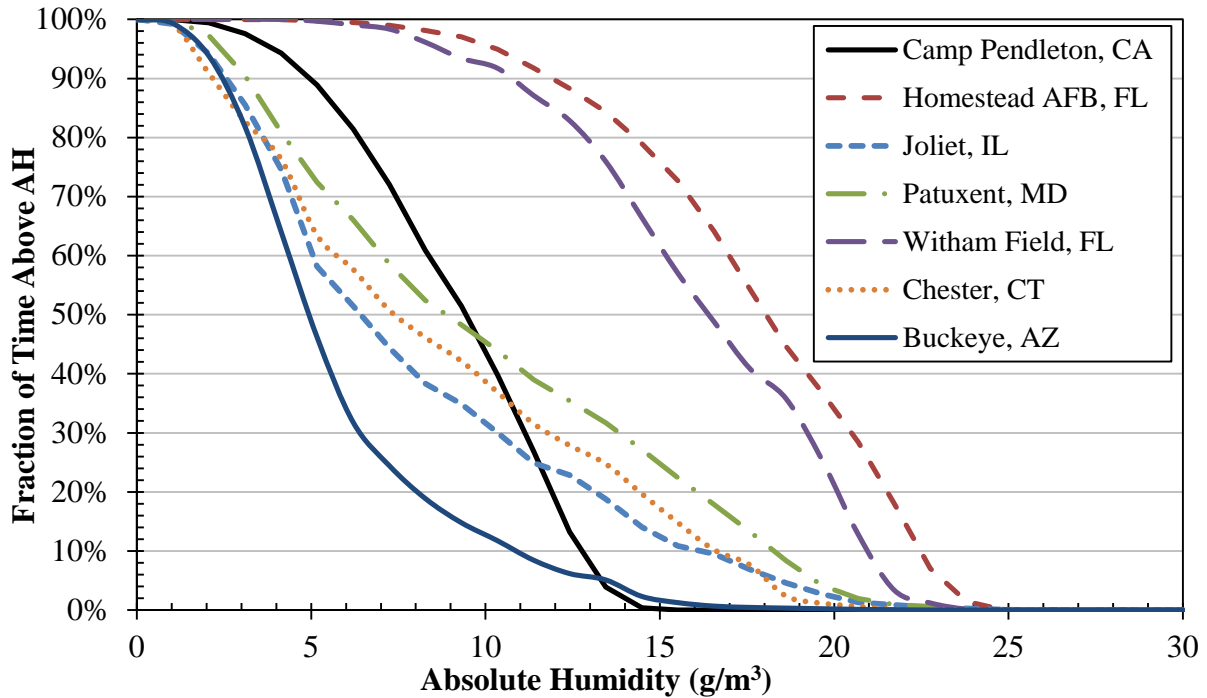


**Figure A-2**  
**Fraction of Year that the Humidity at Different Monitoring Sites [7] is at or above a Given Value of AH**

## A.2 Crack Growth Rate

The crack growth rate equation, as implemented in this assessment, is described in the following sections. The bases for dependencies on different environmental and material factors are also provided.

### A.2.1 CGR Equation Structure

The crack growth rate equation is formed by multiplying factors which account for different environmental conditions with a CGR coefficient. Equation A-2 is similar in form to the SCC crack growth rate equations in MRP-263 [47] and in C-8500 of the ASME Boiler and Pressure Vessel Code Section XI [48]. Common among these equations are a power-law dependence on crack-tip  $K_I$ , an Arrhenius dependence on temperature, and additional factors to adjust the CGR based on the environment. The CGR equation framework for this assessment includes terms to adjust the CGR for expected dependencies on chloride areal density and local relative humidity (aqueous film chloride concentration) as indicated by the structure shown in Equation A-2.

$$\frac{da}{dt} = \alpha (K_I - K_{th})^n f_T f_H f_S \quad \text{Eq. A-2}$$

where

$\alpha$  = SCC crack growth rate coefficient (m/s)

$n$  = stress intensity factor exponent

$K_I = \text{stress intensity factor (MPa}\cdot\text{m}^{0.5})$

$K_{Ith} = \text{stress intensity factor threshold (MPa}\cdot\text{m}^{0.5})$

$f_T = \text{Arrhenius factor of temperature}$

$f_H = \text{CGR dependence factor on humidity}$

$f_s = \text{CGR dependence factor for chloride areal density on the surface}$

Note that the available data shows little dependence on some of these factors, namely chloride areal density and stress intensity factor, resulting in a simplification of the above CGR equation to that shown in Equation A-3.

$$\frac{da}{dt} = \alpha f_T f_H \quad \text{for } K_I > 0 \quad \text{Eq. A-3}$$

When Equation A-3 is averaged over a time, the following relation is obtained:

$$\frac{\Delta a}{\Delta t} = \frac{1}{\Delta t} \int_0^{\Delta t} \left( \alpha \exp \left[ -\frac{Q_g}{R} \left( \frac{1}{T(t)} - \frac{1}{T_{ref}} \right) \right] H(RH(T) - DRH(T)) \right) dt \quad \text{Eq. A-4}$$

where

$$T(t) = T_{offset}(t) + \frac{1}{X} \int_{t-X}^t T_{atm}(\beta) d\beta \quad \text{Eq. A-5}$$

$$RH(T) = \frac{(T)AH}{216.68} 10^{-23.5518 + \left(\frac{2937.4}{T}\right)} (T)^{4.9283} \quad \text{Eq. A-6}$$

$$DRH(T) = \frac{1}{100} \left[ 33.67 - 7.974 \times 10^{-3} (T - 273.15) - 1.090 \times 10^{-3} (T - 273.15)^2 \right] - 0.07 \quad \text{Eq. A-7}$$

$$H(x) = \text{Heaviside step function; } 0 \text{ for } x < 0 \text{ and } 1 \text{ for } x \geq 0 \quad \text{Eq. A-8}$$

$Q_g = \text{activation energy of crack growth (kJ/mol)}$

$R = \text{universal gas constant (kJ/mol/K)}$

$T = \text{temperature (K)}$

Equation A-5 above uses the dummy variable  $\beta$  to calculate the moving average of the atmospheric temperature ( $T_{atm}$ ) over time  $X$ . This moving average, used to represent the canister's thermal inertia, is offset by  $T_{offset}$  to account for the canister thermal power to calculate the surface temperature. The surface temperature is then used to determine the local relative humidity and DRH in Equations A-6 and A-7. In the above equations,  $T_{atm}$  and  $AH$  are defined by the climate data (hourly data is preferred) at or near a given site and  $T_{offset}$  is defined by either measurement or thermal analysis of the canister.

## A.2.2 CGR Equation Parameters

This subsection describes the values chosen for each of the parameters in Equation A-2. Each subsection provides a discussion of the data upon which the value is based and justification for the form of the dependence.

### A.2.2.1 Crack-Tip Stress Intensity Factor Dependence ( $K_{Ith}$ and $n$ )

Review of the existing experimental data in Reference [2] indicates that there is at best a weak dependence on  $K_I$  for crack growth rate. Although initiation testing indicates that time to CISC initiation correlates to the applied stress, the dataset for atmospheric crack growth rates does not currently indicate a significant dependence on stress intensity factor. Consequently, the exponent,  $n$ , in Equation A-2 is taken to be 0.

A power law fit of the atmospheric CGR data presented by Kosaki [5] yields an exponent ( $n$ ) of 0.014. For a  $K_I$  around 10 MPa(m)<sup>0.5</sup>, the power law fit yields a crack growth rate of 0.16 mm/yr and increasing  $K_I$  by a factor of 10 increases the CGR by only 3%. Kosaki also performed accelerated testing using a more expansive set of specimens loaded with NaCl at 60°C and 95% RH. The least-squares fit to a power law for this data yields an exponent of 0.065. Such a low  $K_I$  exponent leads to an increase in the CGR by only 16% when  $K_I$  is increased by a factor of 10. The only other paper which reported CGR values versus stress intensity factor provided only five data points, only one of which (at ~5 MPa(m)<sup>0.5</sup>) indicated a dependence on  $K_I$  relative to data at 10-30 MPa(m)<sup>0.5</sup> [20].

There is precedent for the use of a zero exponent relating  $K_I$  to crack growth. The calculation of Alloy 600 SCC crack growth in BWR environments per ASME Code Section XI uses a zero exponent for  $K_I$  values above 27.5 MPa(m)<sup>0.5</sup> (see Equation 18 of C-8512).

Similarly, there is currently not a supportable threshold value ( $K_{Ith}$ ) above 0 MPa(m)<sup>0.5</sup>. The literature review indicates that unstressed components develop superficial pitting rather than SCC in aggressive marine environments, so low-stress regions remain unsusceptible. No  $K_I$  threshold for crack propagation was observed by Kosaki [5] down to about 1 MPa(m)<sup>0.5</sup> for three point bending specimens with relatively high chloride areal density.

Based on the available data, the stress factor for CGR simplifies to a step function ( $H(x)$ ) with a value of unity for tensile values of  $K_I$ :

$$(K_I - K_{Ith})^n = (K_I - 0)^0 = H(K_I) = \begin{cases} 0 & \text{for } K_I \leq 0 \text{ MPa}\sqrt{\text{m}} \\ 1 & \text{for } K_I > 0 \text{ MPa}\sqrt{\text{m}} \end{cases} \quad \text{Eq. A-9}$$

### A.2.2.2 Temperature Dependence ( $f_T$ )

The temperature dependence of chemical processes, including SCC, is frequently represented by an Arrhenius relationship with a characteristic activation energy. The value of the activation energy can be found by plotting the rate against  $T^{-1}$ . The change in rate from a reference temperature to any other temperature is given by the factor  $f_T$  as described below:

$$f_T = \exp \left[ -\frac{Q_g}{R} \left( \frac{1}{T} - \frac{1}{T_{ref}} \right) \right] \quad \text{Eq. A-10}$$

From the available data, an activation energy is established to describe the effect of temperature on the CGR, and a reference temperature is chosen to normalize experimental data performed at different temperatures. A reference temperature of 80°C is selected for this work since a majority of the CGR data were generated at exposures near this temperature.<sup>6</sup> Within this assessment, the choice of the reference temperature does not affect modeling uncertainty because the crack growth rate coefficient is recalculated when evaluating sensitivities with different activation energies.

Results of crack growth rate tests using 304L compact tension specimens were reported by Shirai of CRIEPI in 2008 [49]; the apparent activation energy for the data is about 80 kJ/mol. The apparent activation energy for 316L CT specimens in Reference [20] is about 190 kJ/mol for that limited data set. Reference [50] showed an activation energy of about 30 kJ/mol for 304 doped with high levels of NaCl. Depending on the test RH, Reference [51] supports activation energies from 25 to 105 kJ/mol, with greatest support for the 30-40 kJ/mol range. This sizable data set for 304 tensile specimens is not used for the shallow CGR coefficient because it also includes initiation time but is sufficiently robust to demonstrate an activation energy dependence, as shown in Figure A-3.

Based on these results, an activation energy of 40 kJ/mol is selected for the model in this report. This value is considered a reasonable average of the different data sets. Sensitivity cases are used to evaluate the effect of activation energy on the crack growth model. Additionally, it is noted that the 80°C reference temperature is higher than the canister surface temperatures where crack growth is expected. Since a lower activation energy results in higher crack growth rates at temperatures lower than the reference temperature, selection of a lower range activation energy is conservative.

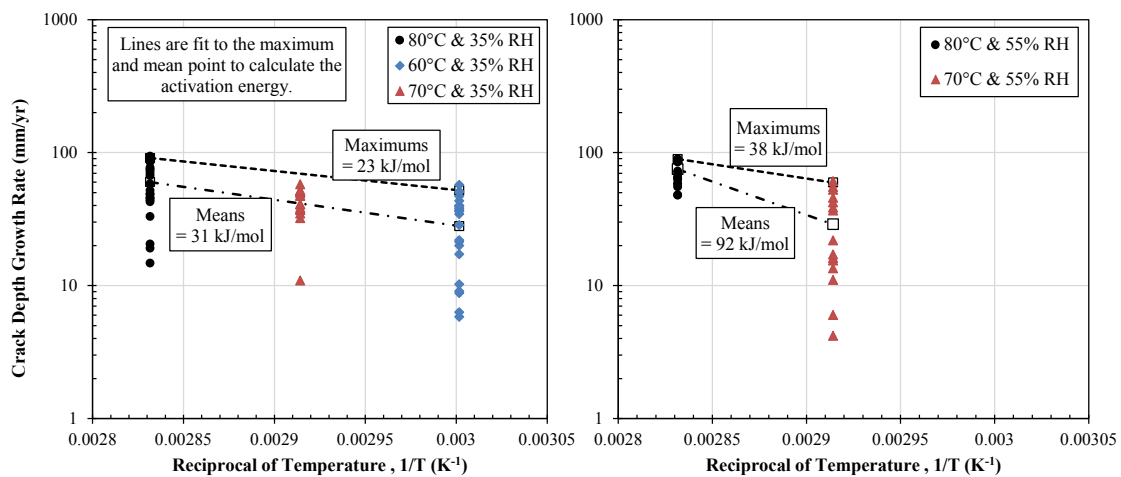


**Figure A-3**  
**Arrhenius Plot for Crack Depth Growth Rate at RH = (Left) 35% and (Right) 55% for the Mean and Maximum Values (Remade from the Data of Reference [52] © NACE International 2008)**

<sup>6</sup> Selecting a reference temperature near these results minimizes the uncertainty in the fitted crack growth rate coefficient if that coefficient is reused with different activation energies without re-normalizing the data to obtain a new CGR coefficient.

### A.2.2.3 Humidity Dependence ( $f_H$ )

The humidity factor,  $f_H$ , is implemented as a step function,  $H(x)$ , which prevents growth when the RH at the surface is less than the calculated DRH value at temperature. The factor, described by Equation A-11, applies a duty cycle to the crack growth rate based on the fraction of time during which the chloride salt is deliquescent and capable of providing an aqueous location on the canister surface for the cathodic half-reaction to occur. There was insufficient data to relate relative humidities above the DRH to crack growth rate with a factor other than unity.

$$f_H(t) = H(RH - DRH) = \begin{cases} 0 & \text{for } RH < DRH \\ 1 & \text{for } RH \geq DRH \end{cases} \quad \text{Eq. A-11}$$

As mentioned in Section A.1.1, this approach uses conservative lower bound DRH values that bound the measured ERH of sea salt in recent testing. A conservative approach to calculating the DRH was taken to account for other factors such as (1) hysteresis in the values of DRH vs. ERH and (2) the finite time required to dry the deliquescent solution once atmospheric conditions change.

The yearly average value of  $f_H$  for the four sites' climate data (utilizing the AH data summarized by Figure A-2) can be calculated for a range of hypothetical canister surface temperatures by integrating the step function in Equation A-11 over time. The fraction of time for which a canister surface at a given temperature experiences humidity above the calculated DRH of sea salt ( $f_H$ ) are plotted in Figure A-4. This example assumes the canister surface maintains a constant offset temperature relative to ambient.

The discontinuous nature of  $f_H$  and the dependence of both the surface RH and the surface temperature on hourly meteorological data mean that the humidity duty factor at a given location is best evaluated at each point in time in conjunction with the Arrhenius factor to yield the time-averaged value of the product  $f_T f_H$ . The time-averaged  $f_T f_H$  is evaluated for a given time interval ( $\Delta t$ ) using Equation A-12.

$$f_T f_H = \frac{1}{\Delta t} \int_0^{\Delta t} f_T(T_{surf}(t)) f_H(T_{surf}(t), AH(t)) dt \quad \text{Eq. A-12}$$

The average product of  $f_T f_H$  for a time period of one year for a range of surface temperatures is shown for various sites in Figure 3-8. The shape of the Buckeye, AZ curve is due to the arid location's combination of high ambient temperatures and low humidity which preclude deliquescence at ambient temperatures for much of the year.

If additional crack growth rate information becomes available in the future, it may be possible to develop a more nuanced model for the dependence of CGR on humidity. In particular, there are data that suggest CGR values decrease at RH values much greater than the DRH [53], corresponding with observed initiation behavior.

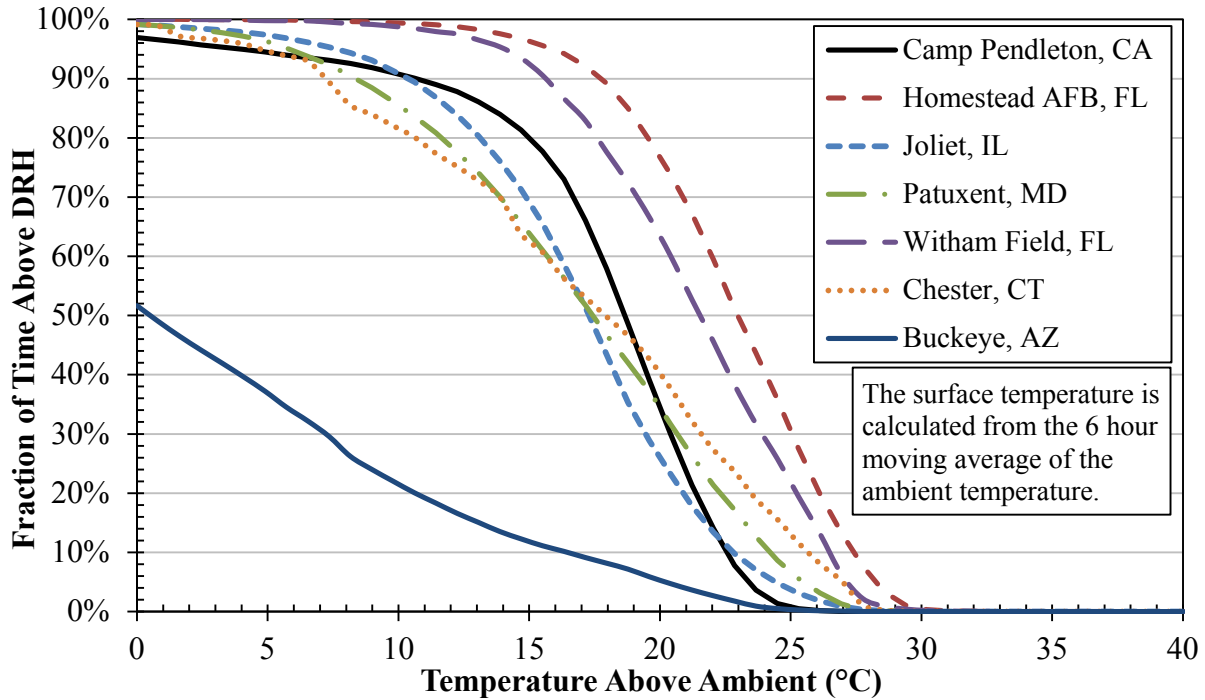


**Figure A-4**  
**Duty Cycle by Baseline Canister Surface Temperature for Coastal Monitoring Stations**

#### A.2.2.4 Dependence on Canister Surface Chloride Areal Density ( $f_s$ )

Currently, the available data are insufficient to develop an explicit dependence for CGR on the areal density of chloride on the surface, so  $f_s$  is set to unity. The  $f_s$  term is mentioned within this technical update as a parameter to be considered if additional CGR data becomes available. It is noted that the crack growth data used to develop the crack growth model coefficient was gathered using relatively high chloride areal density obtained by drying a droplet of sea water (around  $10 \text{ g/m}^2$  [54]). Therefore, it is expected that an  $f_s$  factor, relative to the existing data, would be less than unity.

Initiation testing indicates that the time to SCC crack initiation is dependent on the chloride areal density of the surface, and some dependence would intuitively be expected for crack propagation rates. Albores-Silva [55] reported the maximum crack depths from U-bend specimens were weakly dependent on  $\text{MgCl}_2$  areal density above a threshold of about  $0.5 \text{ g/m}^2$  near the DRH but were a strong function of chloride areal densities above  $1 \text{ g/m}^2$  for RH double the DRH. Effective growth rates can be calculated from the known specimen thickness and time-to-leak data reported by Yajima and Arii [50], but the dependence of the data on the NaCl areal density is substantially different from that of the Albores-Silva data. The sparseness of relevant data and conflicting trends inhibit development of an explicit dependence of the CGR on chloride areal density.

#### A.2.2.5 Crack Growth Rate Coefficients ( $\alpha$ )

Continuous monitoring of crack depth in laboratory experiments by CRIEPI [6] exhibited two-phase crack growth in a manner that suggests partial growth stifling with increasing crack depth. The  $K_I$  values generated by the four-point bending specimens used for the CRIEPI experiments

are calculated later in this section; the results demonstrate that the observed behavior in the CRIEPI experiment is not due to declining  $K_I$  values with depth. Consequently, a second CGR coefficient is derived to include this dependence, and this coefficient is applied once the crack reaches a specific depth.

The anticipated mechanism for a reduction in propagation rate with depth is a limiting of the corrosion current that can be supplied by the cathodic area on the material surface as the crack tip—the anode—moves further away, thereby increasing the ohmic resistance. For immersed specimens, the aqueous cathode area is very large, which generally prevents such a limiting effect. The presence of particulates in the electrolyte layer significantly reduces the cathode capacity (1) through increased ohmic resistance, (2) by interrupting the cathode continuity, and (3) by impeding the transport of oxygen [27]. The partially deliquesced state of sea salt over the most relevant range of RH [8] results in the observed crack stifling behavior. CRIEPI experiments using pure  $MgCl_2$ , which fully deliquesces at 35% RH, did not exhibit the same effect [6]. At very high humidities, the severity may similarly be limited by the increased resistance to the diffusion of oxygen through the surface film as its thickness grows [56]. Smaller and discontinuous deliquescent films limit the cathodic area able to drive the localized corrosion and produce less aggressive environments ([22], [23], and [24]).

Of the data accumulated by the literature review [2], the crack growth rate coefficient fit includes the data which do not include initiation time (experiments using a sharpened pre-crack or continuous measurement) and where the chloride source is sea salt (natural or simulated). Data for atmospherically exposed specimens subject to solar heating is not used due to uncertainty regarding the surface temperature.

Due to the small sample size available for the deep growth rates, statistical analysis of the data is performed to estimate the inherent uncertainty in the data. Instead of directly using a fit to the data to obtain various percentile crack growth rates, the approach explained in Section A.2.3 is used which accounts for uncertainty in the mean and in the distribution of the data.

### **Shallow Growth (First Phase)**

References [20] and [6] reported data from experiments which meet the criteria for inclusion in the first phase CGR coefficient fit. Additionally, the applied loads in these tests generate  $K_I$  values that are comparable to those caused by residual stresses present near welds in the canister. All data are adjusted to a reference temperature of 80°C using an activation energy of 40 kJ/mol.<sup>7</sup>

The included data are for constant humidity and temperature laboratory experiments. The CGR data published by Tani of CRIEPI consists of 316L CT specimens at 35% RH and temperatures of 50°C and 80°C [20]. A drop of seawater was placed inside the machined notch and various  $K_I$  values from 5 to 30 MPa(m)<sup>0.5</sup> were applied. The CGR data in CRIEPI N10035 [6] is summarized in a paper by Shirai [54]. The testing was performed under the relatively aggressive conditions of 80°C, 35% RH, and about 10 g/m<sup>2</sup> as  $Cl^-$  with a tensile stress of about 270 MPa at the surface of a 10 mm thick beam (polished with 600 grit). Both of these tests used potential

---

<sup>7</sup> The 40 kJ/mol activation energy is used for all cases except for sensitivity cases exploring activation energy. In these cases, the data are adjusted using the activation energy specified in the sensitivity case.

drop measurement techniques to continually monitor crack depth. All the sea salt tests in Reference [6] exhibited bilinear growth with an initial growth rate before about 2 mm of depth followed by a slower steady state growth rate; only the shallow CGRs are used for the first phase growth coefficient. Reference [20] contained data at 50°C that were consistent with an activation energy of 190 kJ/mol. These were conservatively omitted because they would significantly reduce the mean value.

While there is a general preference to not explicitly include data that convolves initiation and growth when fitting to a CGR coefficient, it is still important to evaluate these data for consistency with the chosen fit. The data from Shoji [44] for periodic measurement of crack length on U-bend specimens of 304 and 316L held at room temperature and 30% or 40% RH are comparable to the Kosaki data. The data from Hayashibara [51] are for tensile specimens held between 60°C and 80°C for 120 hours; they are consistent with the rapid propagation through the first 1-2 mm of depth seen in N10035 [6] over similar depths. As the data within these references is within the inherent scatter of (and typically slower than) the data set used to develop the CGR coefficient fit, it remains appropriate to not explicitly include initiation-plus-growth data in the statistical fit. The first phase CGR coefficient for shallow crack growth is provided by Figure A-6 in Section A.2.3.3.

### **Deep Growth (Second Phase)**

The CGR observed in the second phase of growth in Reference [6] was lower than the initial CGR by a factor of more than 25. The initial crack propagation rates are used for the first phase CGR coefficient and are consistent with those for similar conditions in Reference [51], in which the short exposure time resulted in crack depths shallower than the transition points in the CRIEPI data. Similar two-phase growth behavior is indicated in testing of a 316L CT specimen—reported in Reference [20]—at 80°C, 10 MPa(m)<sup>0.5</sup>, and 35% RH, but the test was stopped before the second growth phase became fully apparent. The second phase CGR coefficient for deep crack growth is provided by Figure A-7 in Section A.2.3.3.

### **Transition Depth ( $a_{trans}$ )**

The bi-linear crack growth observed in the testing of 304L four-point bending specimens [6] transitions from the first growth rate to the second at a depth that ranged from 1.5 to 2.5 mm in depth. A depth, rather than time, transition point is used due to the expected dependence of crack growth on the capacity of the surface cathode area to supply sufficient corrosion current and because less variability in the transition point is exhibited with depth than time. The transition depth is provided by Figure A-8 in Section A.2.3.3.

### **$K_I$ vs. Depth for Four-Point Bend Specimen**

As noted previously, the laboratory experiments by CRIEPI [6] used four-point bending specimens to load the initiated cracks rather than a compact tension specimen. In order to assess the potential of the bending load to influence the crack growth results, the  $K_I$  as a function of depth was calculated for a flaw in a plate subject to pure bending.

A hand calculation method for calculating the  $K_I$  value for a flaw in a plate subject to pure bending is presented in [57]. The inputs for the calculation are based on the CRIEPI specimen: a 10 mm thick plate subject to a pure bending load resulting in a 270 MPa outer fiber stress. Using

the inputs with a semicircular flaw ( $a/c = 1$ ), the results at the crack tip (deepest point) and at the crack surface point are presented in Figure A-5 below. These results indicate that the  $K_I$  value at the crack tip increases as the crack grows to an  $a/t$  of about 0.2 (2 mm depth for a 10 mm plate), then mostly flattens out until the crack reaches an  $a/t$  of about 0.4 (4 mm depth) where it begins to decrease, eventually reaching 0 at about  $a/t = 0.7$  (7 mm depth). The  $K_I$  value at the crack tip is at its highest in the 2 to 3 mm depth range where the transition between shallow crack growth and deep crack growth occurs.

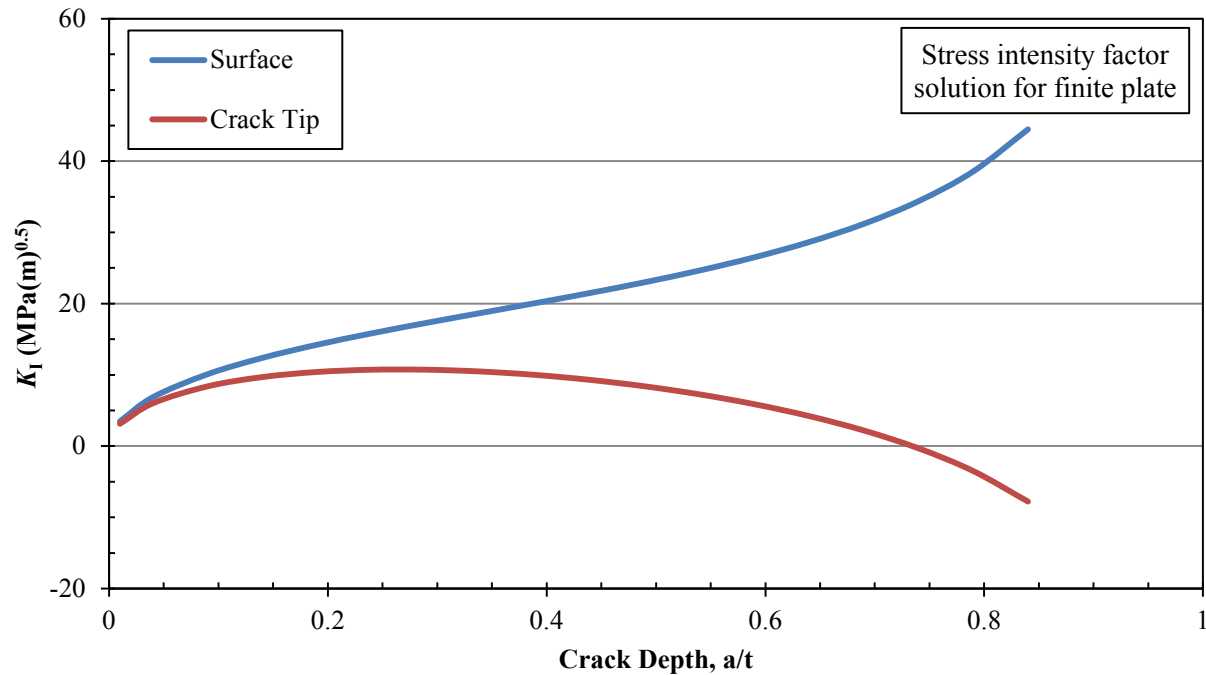


**Figure A-5**  
 **$K_I$  vs. Depth for a Flaw in a Plate 10 mm Thick, Subject to 270 MPa Bending**

### **A.2.3 Statistical Treatment of Growth Rate Parameters**

As described in the prior subsections, the available crack growth rate data is analyzed to determine statistically conservative values for the two crack growth rate coefficients (shallow and deep growth) and the crack growth transition point between them. This section describes the statistical analysis process used to obtain these values in greater detail.

For crack growth rate data, the log-normal distribution is the primary statistical fit used in this assessment. The log-normal distribution is useful for describing a variable for which sampled values are positive, are independent, and vary over multiple orders of magnitude. Log-normal distributions have been applied to describe the CGRs for other SCC mechanisms. Distributions typically used in survival analysis (e.g., Weibull) are less appropriate and others (e.g., normal distribution truncated at zero) provide less satisfactory fits to CGR data.

#### **A.2.3.1 Standard Approach to Fitting Distributions to Data**

After normalizing the data using the relations discussed in the prior sections, the data points are sorted and the empirical cumulative distribution of a crack growth rate occurring is determined.

The cumulative frequency,  $F(x)$ , for the occurrence of the  $i^{\text{th}}$  data point in an ordered set of  $n$  points is given by Bernard's median rank approximation:

$$F(x) = \frac{i - 0.3}{n + 0.4} \quad \text{Eq. A-13}$$

Equation A-13 is used to plot the available data as an empirical CDF to compare with the fitted distribution curves.

For large data sets, distribution parameters are estimated using the maximum likelihood estimators. For a log-normal distribution with the probability density function in Equation A-14, these are defined by Equations A-15 and A-16. For the normal distribution, the  $\ln(x)$  in each of these three equations is replaced by  $x$ , and the  $x$  in the denominator of Equation A-14 is removed.

$$p(x | \mu, \sigma) = \frac{1}{x\sqrt{2\pi\sigma^2}} \exp\left(-\frac{(\ln x - \mu)^2}{2\sigma^2}\right) \quad \text{Eq. A-14}$$

$$\hat{\mu} = \frac{1}{n} \sum_k^n \ln(x_k) \quad \text{Eq. A-15}$$

$$\hat{\sigma}^2 = \frac{1}{n} \sum_k^n (\ln(x_k) - \hat{\mu})^2 \quad \text{Eq. A-16}$$

where

- $x$  = random variable with the t-distribution
- $\mu$  = mean of the distribution of  $\ln(x)$
- $\sigma$  = standard deviation of the distribution of  $\ln(x)$

The use of maximum likelihood estimators ( $\hat{\mu}$ ,  $\hat{\sigma}$ ) is a standard approach for fitting a distribution to data and represents the fit for which the product of the probability of each data point occurring is highest.

#### A.2.3.2 Fitting to Small Populations of Data

Due to the greater uncertainty regarding values for a limited sample size of data, an alternate approach is appropriate when the sample size is small enough that the maximum likelihood estimate of the mean may not correspond to the actual mean of the parameter. The two-stage approach taken to create a more conservative estimate of the parameters' values is described below:

1. Find the maximum likelihood estimates for the mean ( $\hat{\mu}$ ) and standard deviation ( $\hat{\sigma}$ ) in log-space based on the observed sample of crack growth rates.
2. Use the t-distribution to establish a confidence interval on the mean, (and, optionally, the chi-squared distribution to establish a confidence interval on the standard deviation)
3. Use the conservative bounds of the confidence interval to establish a conservative log-normal fit and choose the percentile value for use in the assessment.

### Step 1:

First, the maximum likelihood fit is determined for the dataset. This explanation uses the log-normal distribution, but the method is also applicable to other distributions. Equation A-15 is used to estimate the mean, and Equation A-17 is used (with the Bessel correction, replacing  $1/n$  with  $1/(n-1)$ ) to estimate the sample standard deviation.

$$S^2 = \frac{1}{n-1} \sum_k^n (\ln(x_k) - \hat{\mu})^2 \quad \text{Eq. A-17}$$

### Step 2:

When estimating the true distribution of a parameter from a small sample of data, the average of the data may not correspond to the mean of the parameter. For a parameter which is expected to have a normal distribution, the t-distribution can be used to estimate the true mean of the parameter's distribution based on the samples observed.<sup>8</sup> The conservative bound of this confidence interval can then be used to establish a conservative distribution for the original data.<sup>9</sup> Equation A-18 is used, which adds the product of the sample standard deviation and value of the t-distribution with  $(n-1)$  degrees of freedom at the conservative bound of this confidence interval  $(1-(1-\alpha)/2)$  to the estimated mean [58].

$$\mu_{CI} = \hat{\mu} + ST_{(1-\alpha)/2, n-1} \quad \text{Eq. A-18}$$

### Step 3:

In the third step, the adjusted mean from Step 2 ( $\mu_{CI}$ ) is used to determine an estimated distribution for the dataset by using it in lieu of the estimated mean ( $\hat{\mu}$ ) in Equation A-16 to determine the most likely standard deviation for which the observed data would occur if the true mean were to be  $\mu_{CI}$ . This mean and standard deviation define the log-normal distribution used to determine the various percentile crack growth rates for small data sets.

#### A.2.3.3 Applied Statistics for CGR Coefficient Data

Conservative fits for the shallow CGR coefficient, deep CGR coefficient, and transition depth are obtained by applying the statistical approach of the prior subsection to the data described in Section A.2.2.5. The log-normal distribution is used for the two CGR coefficients while the normal distribution is applied to the transition depth.

For each of the three parameters, the best-fit plots and the fit using the upper bound of the 50 percent confidence interval (75<sup>th</sup> percentile) mean with a fitted standard deviation are plotted against the data in Figure A-6, Figure A-7, and Figure A-8. For the CGR calculations performed in this report, the 95<sup>th</sup> percentile value of this conservatively fit distribution is used.

---

<sup>8</sup> Taking the natural logarithm of each data point in a log-normally distributed data set results in a normally distributed data set. This approach is used to transform the log-normally distributed data into a form for which the t-distribution can be used to estimate the mean.

<sup>9</sup> For a confidence interval of 80%  $(1-\alpha)$ , the upper bound of the confidence interval is the 90<sup>th</sup> percentile  $(1-(1-\alpha)/2)$ .

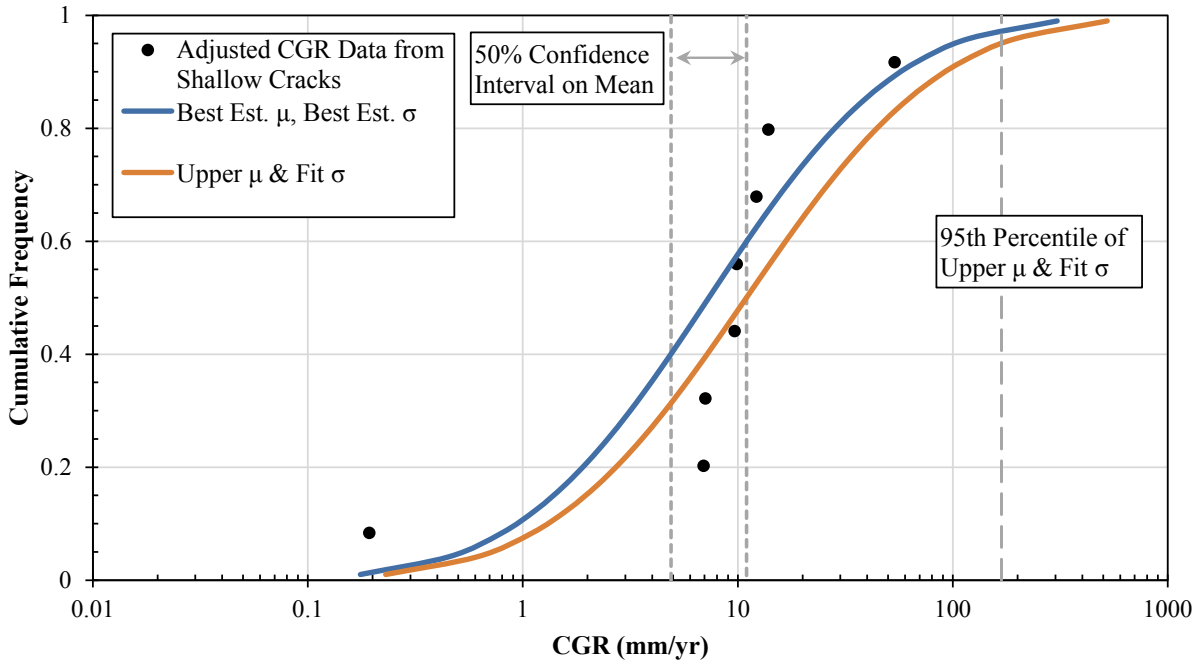


**Figure A-6**  
**Cumulative Log-Normal Distribution for CISCC Experiments Reporting CGR Data for Sea Salt ([20] and [6]), in Shallow Cracks (First Phase Growth)**

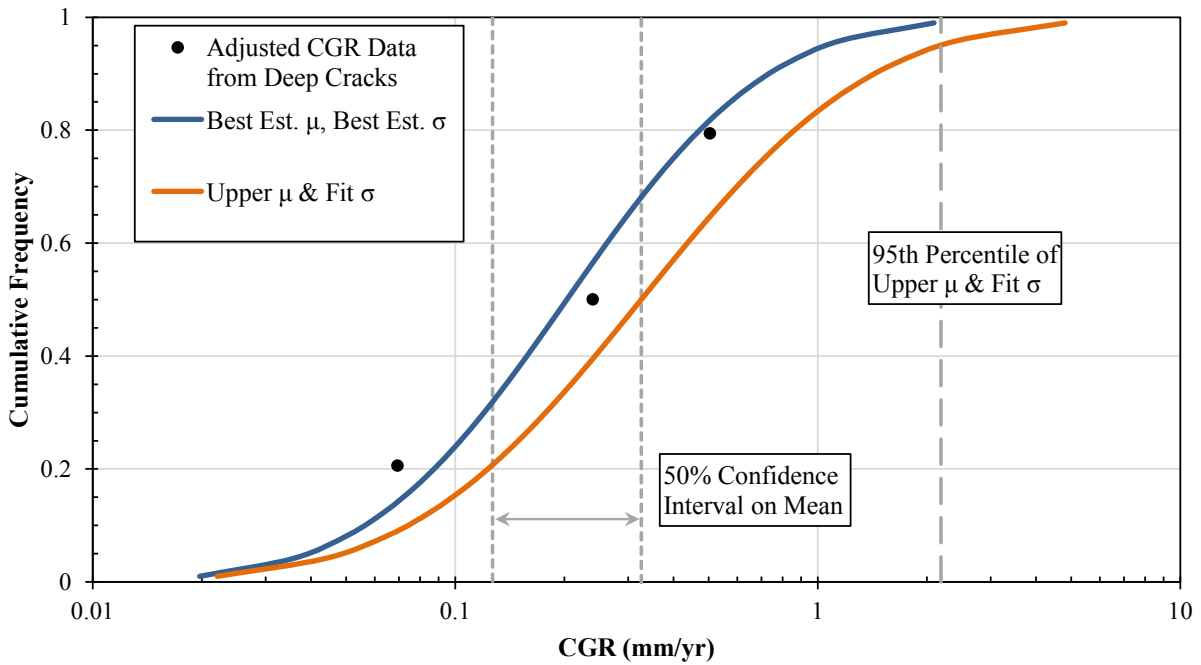


**Figure A-7**  
**Cumulative Log-Normal Distribution for CISCC Experiments Reporting CGR Data for Sea Salt [6], in Deep Cracks (Second Phase Growth)**

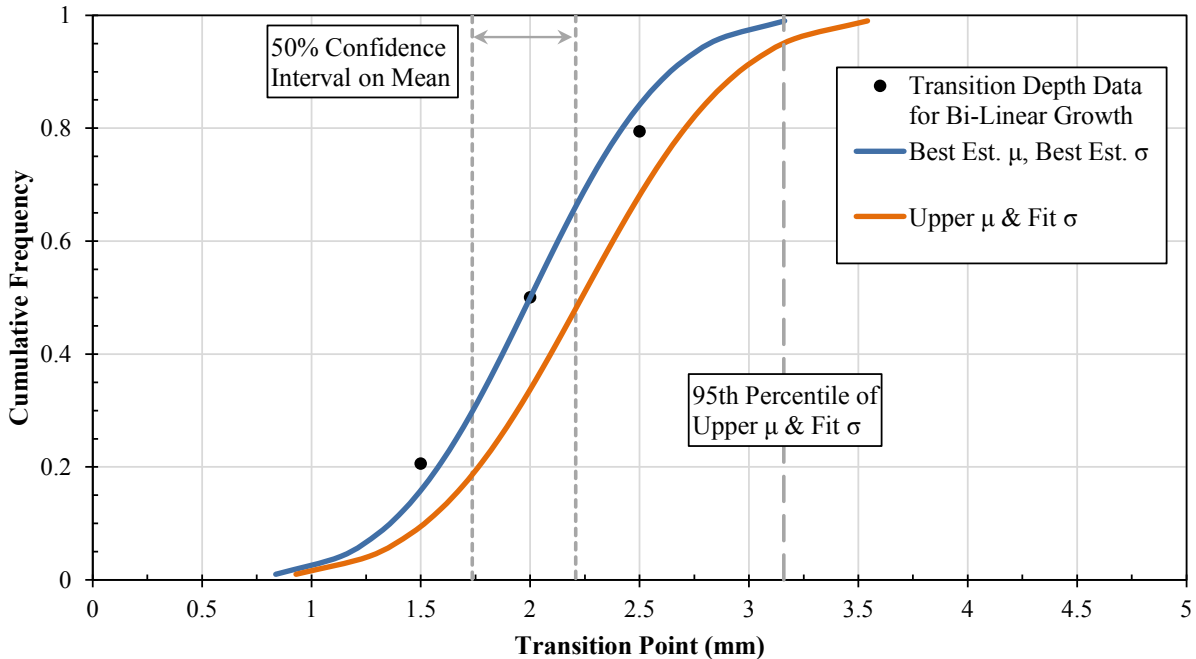


**Figure A-8**  
**Cumulative Normal Distribution for the Transition Depth Seen in CISCC Experiments Reporting CGR Data for Sea Salt [6]**

### A.3 Thermal Analysis Data

Calculations of the canister surface temperature as a function of decay heat are used primarily to provide a reasonable long-term variation in surface temperature during flaw growth calculation. Substantial CFD and analysis work on the thermal-hydraulic behavior of DCSSs has recently been performed by Pacific Northwest National Laboratory (PNNL) ([13], [11], and [16]), and additional analyses of a more bounding nature are present in design SARs (e.g., [15]). Data from these thermal analyses are used to support both the flaw growth and flaw tolerance assessments.

#### A.3.1 Fuel Assembly Decay Power

The calculated decay power is used to reduce the canister temperature over time for crack growth modeling. The decay power of a given assembly is primarily dependent on the time since being discharged from the reactor, the burnup, the initial enrichment, and the mass of fuel in the assembly.

Without pre-determined fuel loadings to consider, this assessment lends itself to the use of generalized models based on curve fitting to computationally modeled decay heats. The decay power at a point in time is calculated using the four term exponential regressions in Appendix C of SAND87-2909 [12]. The report provides calculated decay constants and exponential coefficients for PWR and BWR fuel assemblies over a range of burnup values (PWR from 5 to 60 Gwd/MTHM; BWR from 5 to 40 Gwd/MTHM). The model was developed by curve fitting to the results of ORIGEN2 at 23 points spaced logarithmically from 5 to 1000 years, with 18 points between 5 and 100 years. Very good agreement between the curve fits and the ORIGEN2 results was reported.

Figure A-9 shows example results for the SAND87-2909 [12] model for both BWR (dashed lines) and PWR (solid lines) fuel assemblies for various burnups. Crack growth times are relatively insensitive to the modeled fuel loading when compared with other parameters such as activation energy or initial temperature, so a more comprehensive or complex treatment is not warranted.

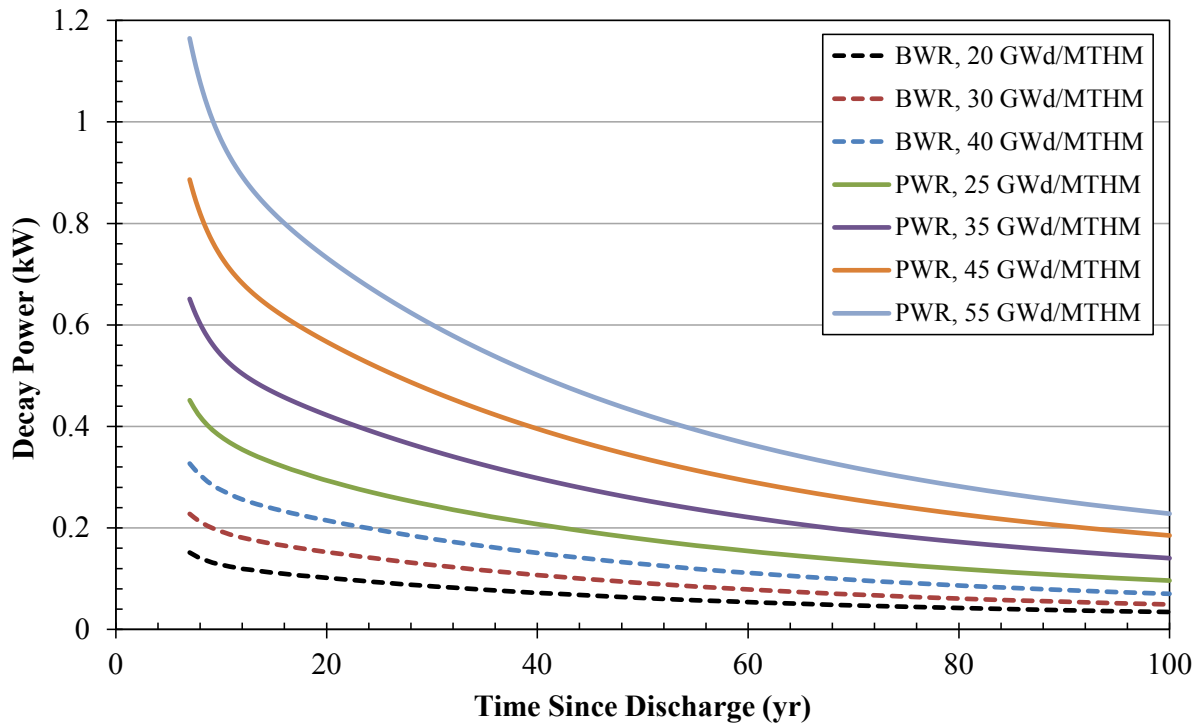


**Figure A-9**  
**Decay Power per Assembly Curves for Different Burnups of PWR and BWR Fuel**

### A.3.2 Canister Temperatures

The evaluations in the report are presented primarily in terms of the surface temperature rather than the location on the canister surface, since different locations on a canister surface reach the various key surface temperatures at different times. As mentioned in the assumptions in Section 2, surface temperatures that result from different decay heat power values are obtained by scaling the difference between the ambient and canister surface temperatures. Consequently, defining the temperature profile for a given canister at a given thermal power is unnecessary. Additional information on canister surface temperatures for different design types is available from literature sources; this information is summarized in the following paragraphs.

For horizontal canisters, the results from Figure 7.5 of PNNL-21788 [13] and the contour plot of Figure 7.3 of that same report provide surface temperatures at 7.6 kW. Similarly, the contour plots in Reference [14] provide surface temperatures at 24 kW (albeit for a different canister model). For vertical canisters, the temperature is approximately axisymmetric, and the axial temperature profiles in Appendix A of PNNL-22552 [16] and in SAR analyses provide the form of temperature variation on vertical canisters. The shape of the temperature profile is relatively

consistent across designs. Consideration of these surface temperature profiles permits the reader to consider the canister regions over which crack propagation may occur at a given power level.

PNNL-21788 [13] and design SAR analysis also provide internal temperature profiles. Adjusted to be within the expected power range at the time of shell penetration, these profiles support the internal gas temperatures assumed for Section 4.2 analyses. Temperatures after depressurization or air ingress would rise, but internal temperature has a small enough effect that omission of such dependencies is a relatively minor assumption.

## A.4 Gas Transmission Between Canister and Environment

This section describes the models used to characterize gas transmission between the canister interior and exterior.

### A.4.1 Leak Rate

The leakage model used is based on EPRI 1011820 Appendix D [9] and is modified to include a term that accounts for the tortuosity of SCC crack morphology. The bend loss coefficient accounts for the tortuous nature of SCC cracks by adding a pressure loss dependent on the number of 45° or 90° turns along the path of a crack, as implemented in the SQUIRT code for leak rate calculation [10].

This model for flow rate through a crack is used to calculate the decay of the helium internal pressure and helium mole fraction. The crack area is assumed to be constant through-wall for the purpose of this calculation and flow is assumed to remain laminar and incompressible.

$$\begin{aligned}
 \Delta P_{\text{laminar losses}} &= \frac{12\mu a}{L^2 A} q \\
 \Delta P_{\text{entrance}} &= \left( \frac{0.5\rho_{\text{in}}}{2A^2} \right) q^2 \\
 \Delta P_{\text{exit}} &= \left( \frac{1.0\rho_{\text{out}}}{2A^2} \right) q^2 \\
 \Delta P_{\text{tortuous}} &= e_v \left( \frac{\rho_{\text{in}}}{2A^2} \right) q^2 \\
 \Delta P &= \left( \frac{\Delta P_{\text{laminar losses}}}{q} \right) q + \left( \frac{\Delta P_{\text{entrance}}}{q^2} + \frac{\Delta P_{\text{exit}}}{q^2} + \frac{\Delta P_{\text{tortuous}}}{q^2} \right) q^2
 \end{aligned}
 \tag{Eq. A-19}$$

where

- $\Delta P$  = pressure drop (Pa)
- $\mu$  = viscosity of helium (Pa-s)
- $L$  = crack opening (m)
- $a$  = crack depth (shell thickness) (m)
- $A$  = crack area (m<sup>2</sup>)
- $q$  = volumetric flow rate (m<sup>3</sup>/s)
- $e_v$  = bend loss coefficient

The quadratic equation is used to solve the last line of Equation A-19 for the flow rate. The gas properties used in this analysis are taken from Reference [59].

#### ***A.4.2 Ingress due to Temperature and Pressure Fluctuations***

The high thermal mass of the canister/overpack system provides the potential for pressure differences between the ambient and canister internal volume based on diurnal and seasonal temperature variations. These variations can cause a breathing or pumping effect that drives replacement of the helium backfill with air faster than by diffusion alone.

The calculation in Section 4 iteratively solves for the internal pressure, internal moles of air and helium, and leak rate through the crack. Using the ideal gas law and the moles of gas inside the canister, the pressure differential across the crack is determined for a given external pressure and average internal gas temperature. This pressure is used as described in the prior section to determine the flow rate through the crack into or out of the canister. For flow from the canister, the mole fraction of helium in the escaping gas is the average mole fraction of the gas within the canister. The leak rate is applied linearly over each time step, and the volume of gas leaked is limited for a given time step to the volumetric change associated with the change in pressure and temperature.

For large crack areas, the loss rate is limited by the cyclic volumetric expansion rather than the flow rate through the crack. For these cracks, atmospheric fluctuations on timescales smaller than an hour are not accounted for, and the rate of air ingress may be somewhat underestimated. For tight flaws, the flow rate calculated using Equation A-19 severely restricts the rate of helium loss.





**The Electric Power Research Institute, Inc.** (EPRI, [www.epr.com](http://www.epr.com)) conducts research and development relating to the generation, delivery and use of electricity for the benefit of the public. An independent, nonprofit organization, EPRI brings together its scientists and engineers as well as experts from academia and industry to help address challenges in electricity, including reliability, efficiency, affordability, health, safety and the environment. EPRI also provides technology, policy and economic analyses to drive long-range research and development planning, and supports research in emerging technologies. EPRI's members represent approximately 90 percent of the electricity generated and delivered in the United States, and international participation extends to more than 30 countries. EPRI's principal offices and laboratories are located in Palo Alto, Calif.; Charlotte, N.C.; Knoxville, Tenn.; and Lenox, Mass.

Together...Shaping the Future of Electricity

© 2014 Electric Power Research Institute (EPRI), Inc. All rights reserved.  
Electric Power Research Institute, EPRI, and TOGETHER...SHAPING THE  
FUTURE OF ELECTRICITY are registered service marks of the Electric  
Power Research Institute, Inc.

3002002785